Article

Performance, Efficiency, and Flexibility Analysis of a High-Temperature Proton Exchange Membrane Fuel Cell-Based Micro-Combined Heat-and-Power System with Intensification of the Steam Methane Reforming Step by Using a Millistructured Reactor

Di Wu,* Jean-Marc Commenge, Emilien Fort, Claire Hardy, Jérôme Pecquery, and Laurent Falk

Read Online

ACCESS | Metrics & More | Article Recommendations

ABSTRACT: The complete simulation model of an existing 1 kW high-temperature proton exchange membrane (HT-PEM) fuel cell-based residential micro-combined heat-and-power process, including a compact intensified heat-exchanger-reactor, is developed in the simulation software ProSimPlus v3.6.16. Detailed simulation models of the heat-exchanger-reactor, a mathematical model of the HT-PEM fuel cell, and other components are presented. The results obtained by the simulation model and by the experimental micro-cogenerator are compared and discussed. To fully understand the behavior of the integrated system and assess its flexibility, a parametric study is performed considering fuel partialization and important operating parameters. The values of the air-to-fuel ratio = [30, 7.5] and steam-to-carbon ratio = 3.5 (corresponding to net electrical and thermal efficiencies of 21.5 and 71.4%) are chosen for the analysis of inlet/outlet component temperatures. Finally, the exchange network analysis of the full process proves that the process efficiencies can still be increased by further improving the process internal heat integration.
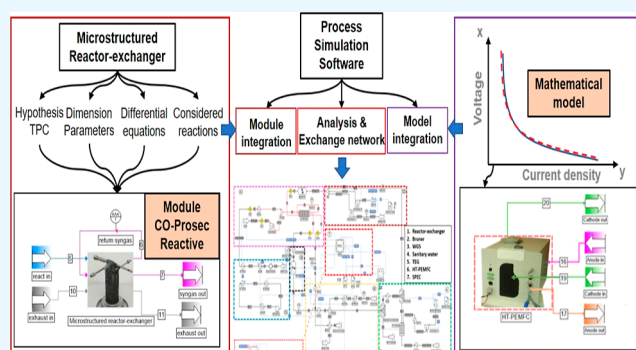
1. INTRODUCTION

Global warming is a severe environmental issue that has drawn the attention of the scientific community to propose reduction strategies of carbon dioxide emissions related to their numerous sources. Among these sources, buildings account for about 40 and 36% of the total European energy consumption and greenhouse gas (GHG) emissions respectively.[1] Around 75% of the total European building floor area corresponds to residential buildings,[2] where the vast majority (up to 80%) of energy use and emissions are related to heating applications.[3] According to the French Ministry of Ecological Transition, the building sector represented around 43% of the overall energy consumption in France in 2020, and buildings were responsible for 23% of GHG emissions.[4] Since 1974, several successive thermal regulations have been set up. For example, RT2012, resulting from the Grenelle environment forum, already set high performance requirements in terms of building conception, comfort, and energy consumption as well as resource requirements.[5] The most recent policy, RE2020, has set more stringent energy efficiency regulations for buildings constructed in France after January 1st, 2022, requiring all new buildings to have a positive or zero energy balance.[6] To achieve the regulation's goal, three technical solutions are chosen, which are able to satisfy the new

constraints: solar photovoltaics, small wind turbines, and micro-combined heat-and-power systems (micro-CHP systems).[7] These proposals allow new buildings to be equipped with their own electrical production. While solar and wind power are confronted with substantial constraints (intermittency, integration in the urban landscape, low acceptance by customers, problem of reliability and performance, requirement of large surface areas, etc.), micro-CHP systems constitute a solution with installation and maintenance similar to that of common boilers, without the constraints of outdoor installation while allowing to stabilize the electrical supply network.[8] For domestic applications, in the case of solar photovoltaics, the unit must be close to the place of use to reduce transmission losses, which is not always easy to achieve due to the size of the modules. Moreover, in case of insufficient radiation or during the night, an auxiliary (e.g., natural gas burner) energy converter is required

to maintain the system in operation. For the electricity generated in power stations, an extensive network is used for electricity transport: power losses generated by Joule effect in transmission lines are a common issue. These losses are more significant than those caused by gas transport in pipelines. Therefore, local power generation is an effective solution to minimize losses. Moreover, while designing a cost-effective net-zero energy building with on-site generation, energy efficiency should be prioritized over renewable power.[7]

Since the 1990s, micro-cogeneration or micro-CHP has been proposed as a possible alternative to gas-fired boilers for households.[9] CHP systems include a prime mover (i.e., reciprocating engine, microturbine, or fuel cell), a generator, heat recovery equipment, electrical switchgear, emissions control devices, and controls (Figure 1).[10] In terms of system
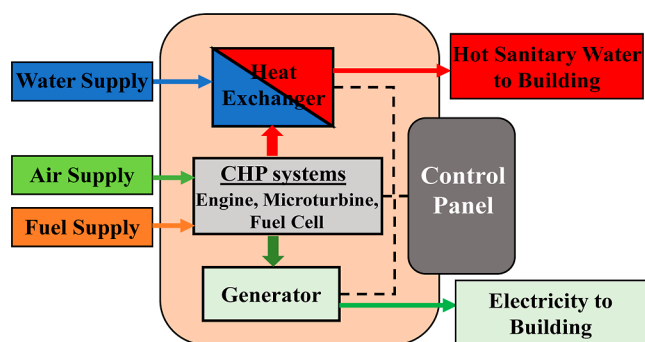

Figure 1. Schematic view of CHP systems.

efficiency, for the same production of electricity and heat, CHP systems require 30% less primary energy compared to central production plants. Renau et al.[11] demonstrated that the fuel-cell-based CHP systems are appropriate to provide the energy demand for heating and hot water in buildings, showing a decrease in both primary energy consumption and CO_2 emissions, even if the hydrogen is obtained from natural gas reforming. The gain in energy efficiency immediately translates into economic and environmental gains through a 30% reduction in the associated GHG emissions.[12] At the scale of a national energy network, these systems reduce the effects of peak loads and ensure continuous availability. They strengthen the energy independence of the network and the integration of intermittent renewable energies.[13] CHP is a well-established technology for large-scale commercial and industrial applications. Therefore, the possibility of developing smaller-scale

micro-CHP units could become a successful solution in the residential building sector. The availability of natural gas supplies in most buildings provides the opportunity to easily replace existing gas boilers, providing electricity and heat simultaneously.[14] According to the European definition (2004/8/CE directive of the European parliament), the term "micro" covers a power up to 50 kWel.[8] Compared to the statistical analysis performed at the EU level, the average annual specific consumption per m^2 for all types of residential buildings was around 0.0021 kW/m^2 in 2013: a micro-CHP system can, therefore, cover the needs of a surface equivalent to 23,800 m^2 of residential buildings.[15] The heart of a micro-CHP unit is the energy converter, which can consist of internal combustion systems (diesel engine and gas turbine), external combustion systems (organic Rankine cycle, steam turbine, and Stirling engine), or fuel cell systems. In this converter, the chemical energy of the fuel is transformed into mechanical (motor, turbine, etc.) or electrical (fuel cell) energy. The electricity produced is shaped to correspond to the voltage of the intended uses. The heat is recovered by a combination of heat exchangers that allow to heat the water of the heating circuit and domestic hot water.[8]

The internal combustion engine produces mechanical energy from the expansion of the gas during the combustion. For micro-CHP applications, the engine operates an electrical generator, and the heat is recovered from the exhaust gas, cooling water, and oil. There are two categories of internal combustion engines: (i) gasoline engines, functioning with the diesel thermodynamic cycle, can be operated with biodiesel, domestic oil, or heavy oil as resource and (ii) spark ignition engines, describing the Otto thermodynamic cycle, preferentially use natural gas or biogas but can also operate with gasoline. The latter have a lower power-to-heat ratio than diesel cycles, but a higher overall energy efficiency. Unlike the internal combustion engine, where the fuel is burned in the combustion chamber and converted into mechanical energy, the Stirling engine operates in a closed circuit, with an external heat supply, usually provided by a burner operating on natural gas, wood, or oil. Working gas transfers allow the recovery of mechanical energy through the movement of pistons, which power an electrical generator.[8,14] The Stirling engine obeys Carnot's law, the maximum efficiency depending on the temperatures of the hot and cold sources. However, the mechanical efficiencies obtained are higher than those of internal combustion engines and can reach up to 40%.[16] The fuel cell is an electrical generator that differs from previous models in the sense that the fuel is transformed directly into

Table 1. Description of the Typical Characteristics of CHP Systems[9,14,20]

| prime mover of micro-CHP system	internal combustion engine	Stirling engines	PBI-based PEMFC	SOFC
electrical efficiency (%)	~25	up to 16	~40	up to 60
overall efficiency (%)	~90	92−95	~90	~85
power range (kWel)	1.5−3	1	5	1.5
size ($w \times d \times h$, mm^3)	760 × 1370 × 1085	490 × 422 × 950	670 × 920 × 1760	600 × 660 × 1010
advantages	multifuel capabilities, high power-to-weight ratio	long maintenance-free operating periods, quieter than internal combustion engines	high electrical efficiency, rapid start-up, high power density, proven technology, low emissions	high electrical efficiency, simple water management, enhanced kinetics, simple fuel processing
disadvantages	high level of pollutant emissions	lower weight-to-power ratio	short lifetime	slow start-up and shut-down procedures, complicated heat recovery
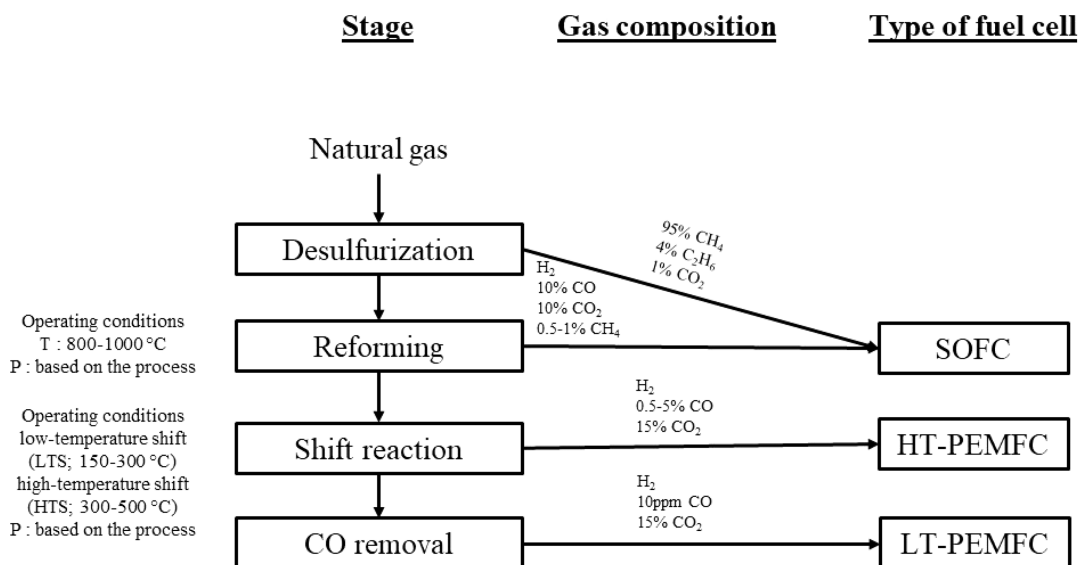
Figure 2. Stages of preparation of the fuel fed to the cell according to the type of cell; SOFC: solid oxide fuel cell, HT-PEMFC: high-temperature proton exchange membrane fuel cell, and LT-PEMFC: low-temperature proton exchange membrane fuel cell.

electricity, without going through a mechanical conversion stage. Fuel cells are recognized as one of the most promising electricity generation technologies.[9,17,18] In comparison to heat-engine-based micro-CHP systems, fuel-cell-based systems offer higher efficiency, higher power-to-heat ratio, quieter operation, simple maintenance routine requirements, and efficient part-load performance. Two important criteria are considered to characterize the fuel cell-based micro-CHP system: the net electrical efficiency is defined as the ratio of the net power output to fuel chemical energy input, and the efficiency of the system is defined as the ratio of the total electricity and useful thermal energy output of the system divided by the fuel chemical energy input (given in Section 2.7). The electrical efficiency of fuel cells can reach up to 60%, instead of 25% in the case of heat-engine-based technology, and the system can attain an overall efficiency of 85−90%.[14] In addition to high efficiencies, the fuel-cell-based CHP systems have the ability to modulate their power output, by promoting either electrical or thermal power. Moreover, since these systems can be operated at lower heat-to-power ratios, excess heat generation is avoided. The configuration of a fuel-cell-based micro-CHP system may vary, as it strongly depends on factors such as the fuel-cell type, the fuel, and the required application.[19]

A summary of the main characteristics of the main representative types of micro-CHP systems mentioned earlier, distinguished by the type of prime mover, is given in Table 1. The electrical efficiency of reciprocating internal combustion engines is higher compared to those of micro-turbines and Stirling engines.[14] On the other hand, fuel cells promise to offer the highest electrical efficiency for residential and small-scale cogeneration applications in comparison with the other technologies. Moreover, fuel cells, by nature of their lack of a combustion process, have extremely low emissions of NO$_x$ and CO. Their CO$_2$ emissions are also generally lower than those of other technologies due to their higher efficiency.[20]

Figure 2 shows the different levels of maturity and operating constraints that affect the fuel-cell-based micro-CHP process. The most promising fuel-cell types are proton exchange membrane fuel cell (PEMFC) and solid oxide fuel cell (SOFC) technologies.[21]

PEMFC technology is very promising for micro-CHP systems because of a number of advantages with respect to SOFC, such as rapid start-up (due to operation at low temperatures), high power density, and low emissions.[22] There are significant shortcomings in the use of low-temperature fuel cells related to the fact that reforming systems suffer from CO concentrations: a concentration below 5 or 10 ppm is required to avoid poisoning of the catalyst layer. The high-temperature PEM fuel cells (HT-PEMFC) are commonly termed HTPEM (or intermediate temperature PEM) and the higher operational temperature increases the efficiency significantly. They can stand higher levels of CO, making the micro-CHP system simpler. Water management is, however, problematic, especially in the case of Nafion-based PEMFCs, due to the phase change of the reaction products: polybenzimidazole (PBI)-based PEMFCs have been developed with a view on simpler water.[23,24] PBI−PEMFCs operate at slightly higher temperatures (140−180 °C vs 60−80 °C for Nafion−PEMFCs)[25] and are capable of operating with lower-quality hydrogen, as compared to a Nafion-based system.[26]

A critical unit in micro-CHP systems is the reforming step. The industrial-scale operation of energy-intensive reactions, such as endothermic steam methane reforming (SMR), is challenging due to ineffective heat transfer from the external burners to the packed catalyst beds.[27] It is obvious that thermal integration of the process is an important strategy to improve the overall energy efficiency of the system. Regarding this aspect, the use of structured heat-exchanger reactors should improve the energy integration of the entire system. The intensification of the SMR step by using microstructured reactors should enable us, on the one hand, to resolve the heat losses problem and, on the other hand, to reduce substantially the size of process units, their energetic consumption, and environmental impact.[28] Among the levers of improvement of the systems of micro-CHP, several other strategies can be identified such as the nature of the catalyst, its mode of deposit inside the reactor, and the internal geometry, which includes the internal structure and the spatial dimensions of the reactor. Thanks to the internal structures and spatial dimensions of microstructured reactors, heat transfer is enhanced and more efficient.[28,29] Intensified heat-exchanger
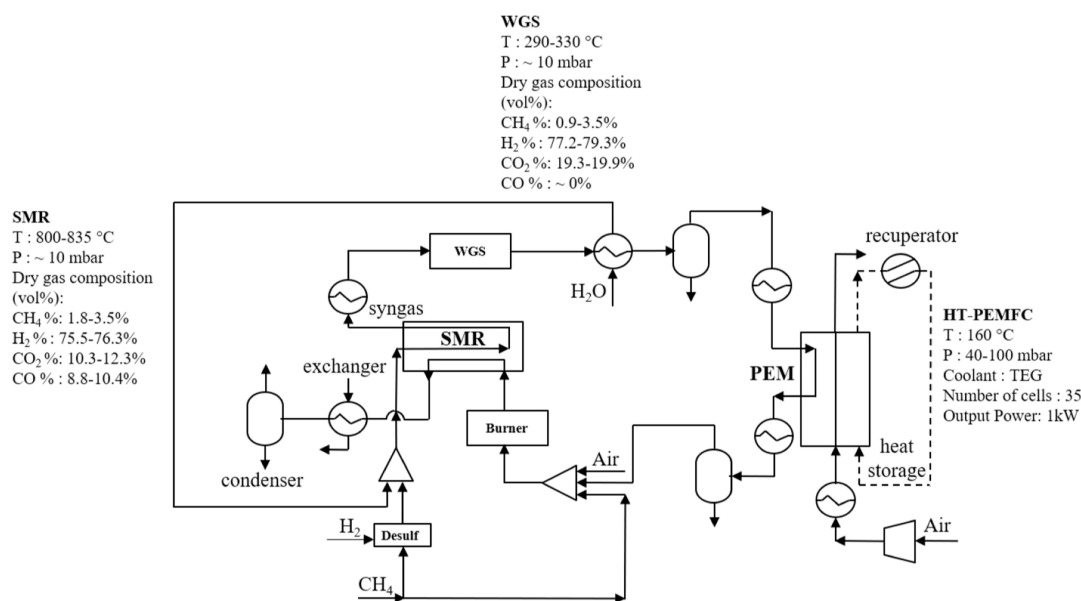
Figure 3. General layout of the experimental micro-CHP process.

reactors appear as a technology adapted to the design of compact and integrated modules, allowing the development of more efficient micro-CHP systems, to satisfy the demand of a new and rapidly growing market.

Several research activities have investigated the application of HT-PEM fuel cells for CHP and micro-CHP purposes. Najafi et al.[30] performed a mathematical modeling and parametric study on a 30 kWel HT-PEM fuel-cell-based CHP system in a residential environment. The electrical and thermal performances of the system have been determined and compared to the performance indices achieved for the previous plant: the net electric efficiency reaches 29.21% (based on LHV), which is obviously high compared to the electric efficiency of LT-PEM fuel-cell-based system of 21.18%. In another study,[31] the authors applied fuel partialization (i.e., changing fuel input) and power-to-heat shifting (i.e., altering the anodic stoichiometric ratio) strategies on the same plant to investigate the capability of the system to deal with intermittent electrical and thermal profiles. Gwak et al.[32] conducted a performance and efficiency analysis on a phosphoric acid-doped PBI membrane HT-PEMFC based tri-generation system. The HT-PEMFC stack model was simplified from a three-dimensional HT-PEMFC model.[33−35] Their results revealed that, as the stack current density was increased from 0.2 to 0.65 A cm^{-2}, the electric efficiency of the HT-PEMFC stack dropped from 33.4 to 26.8%. In addition, a burner equivalence ratio (ER) of around 0.75−0.8 was suitable to achieve higher overall combined heat, cooling, and power (CHCP) efficiencies ranging from 70% at 0.65 A cm^{-2} to 75% at 0.2 A cm^{-2} without any loss of cooling capacity.

The aim of the present work is to combine process simulation in the ProSimPlus v3.6.16 software and experiments to analyze the feasibility and flexibility of a micro-cogenerator as a solution to energy transition applied to novel individual buildings, focusing here on a HT-PEMFC-based 1 kWel micro-CHP system including a Taylor-designed microstructured heat-exchanger-reactor for intensification of the steam reforming step. The model of the heat-exchanger-reactor is developed separately from the entire HT-PEMFC micro-CHP system by solving the mass, heat, and momentum equations considering the geometrical parameters of the device and kinetic character-

istics of the reactions. A mathematical model of the HT-PEMFC unit is identified from experimental measurements of the polarization curve. Then, the integration of these unit models in a complete process simulation is performed and validated, by comparison with the experimental data from the micro-CHP pilot plant. In order to investigate the behavior, performance, and flexibility of this highly integrated system and to determine the optimal operating conditions required for yielding higher efficiencies, a sensitivity analysis of the key parameters is conducted.

Concerning the outline of the study, as a preliminary step, the HT-PEM fuel-cell-based micro-CHP plant has been described in detail. The developed models of the different modules and sub-systems are then presented. Finally, the results from experimental and numerical approaches are compared and discussed.

2. MATERIALS AND METHODS

The present section will successively present the experimental CHP plant and the individual unit models for the reforming heat-exchanger reactor and the fuel-cell stack, before combining these models in the numerical simulation of the complete plant. The heat integration system at the process scale will be described and the overall performance indices defined.

2.1. Description of the Experimental System. The experimental CHP plant is composed of a methane steam reformer to generate hydrogen, and a shift reactor to increase the hydrogen content in order to supply the membrane fuel cell (Figure 3).

The off-gases of the fuel cell are injected into a burner to provide the necessary heat and to feed the reformer with superheated steam. All these elementary operations [SMR, water-gas-shift (WGS), stack, burner, and vaporizer] exchange heat and mass so that the system performance is strongly dependent on the quality of the coupling between these operations. The use of microstructured heat-exchanger reactor for this application aims at improving the system energy integration, reducing the spatial dimensions and stabilizing its operation.
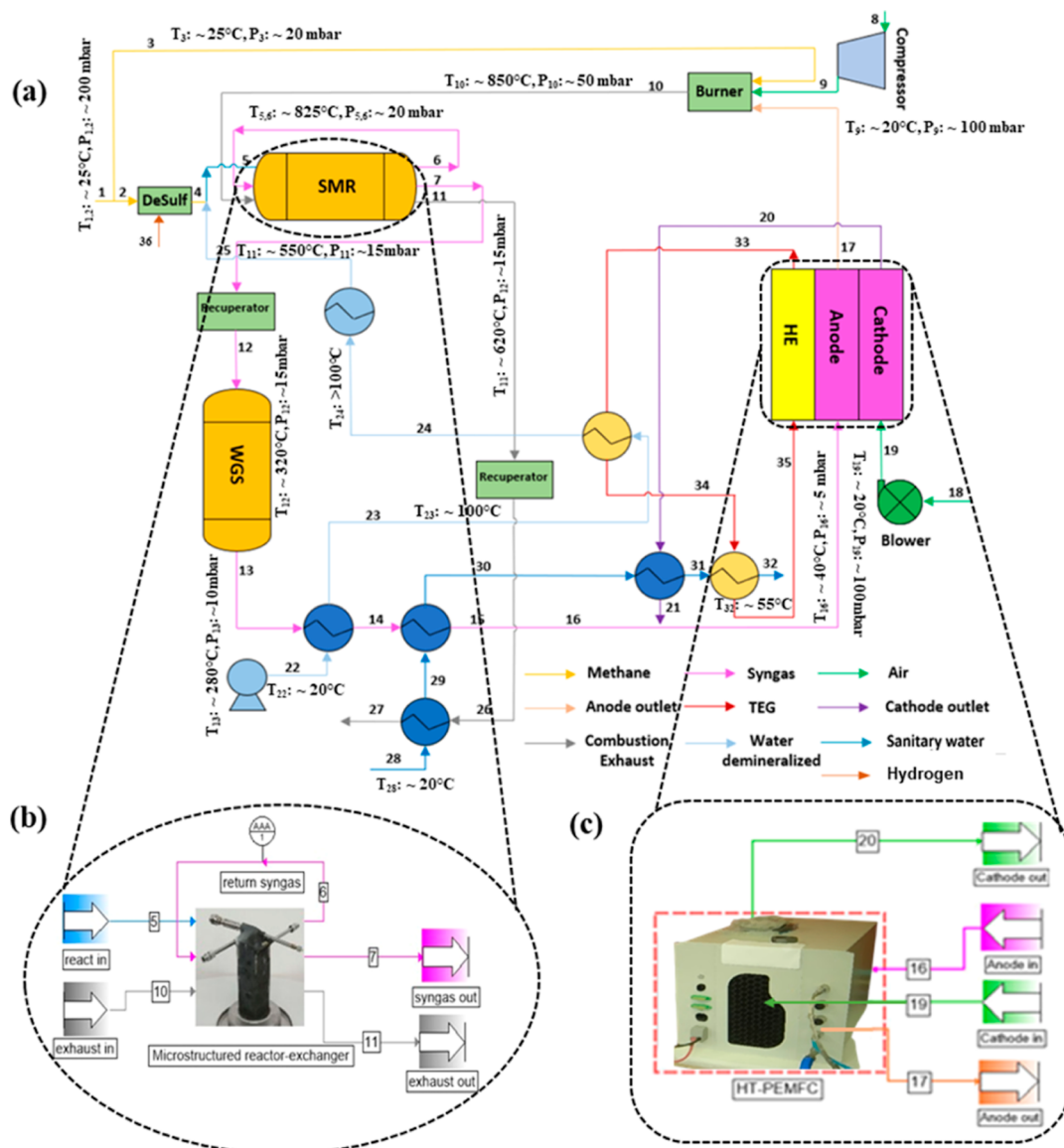
Figure 4. (a) Detailed view of the HT-PEMFC-based plant, (b) equipment diagram of the heat-exchanger reactor, and (c) HT-PEMFC.

Figure 4a shows the process configuration of the HT-PEMFC-based CHP plant with thermal integration, which is fed by natural gas (stream 1). Before entering the heat-exchanger reactor, the fuel is divided into two streams: on one hand, natural gas is desulfurized (stream 2) to reach the acceptable level of sulfur content before steam reforming to protect the catalyst, and on the other hand, a fraction of the feed is sent to the catalytic burner (stream 3). The fuel leaving the desulfurizer is mixed with superheated steam (stream 25), which is preheated first by the triethylene glycol (TEG) circulation unit and then by a vaporizer before mixing with the fuel. The mixture of natural gas and steam enters the microstructured heat-exchanger reactor (stream 5) where the catalytic SMR reaction takes place to produce hydrogen, carbon monoxide, and carbon dioxide with a part of unreacted feed components.

Since this reaction is endothermic, high temperatures (approximately 800 °C) promote the reaction in the sense of production of hydrogen. The heat required in the SMR unit is provided by combustion gases from the catalytic burner (stream 10). The heat-exchanger reactor, whose design is detailed in Section 2.2, is developed using 3D additive manufacturing

technology: its internal structure is composed of parallel channels, dedicated either to the reactive mixture or to the heating fluid. Since the SMR is a catalytic reaction, the flow passages for the reactants have been coated with rhodium-based catalyst.[28] The pressure drop through the SMR is not significant, and the limitations by mass transfer in the catalyst layer are minimal. The milli-structuring of the channels also allows an enhanced transfer of chemical species from the fluid to the surface of the catalyst, strongly decreasing the limitations by external mass transfer.

The exhaust gases (stream 10) with an average temperature of 800 °C, coming from the catalytic burner, provide heat not only for the endothermic reaction but also to preheat the feed mixture. In addition, to improve internal heat integration, the hot syngas is recycled back to a non-catalytic set of channels to provide sensible heat to the reaction. As the temperatures of outlet streams of the heat-exchanger reactor (syngas: stream 7; combustion gases: stream 11) are still high, their available thermal energy is recovered as a heating resource for steam vaporization and at the reactor and cathode inlets.

Although the tolerance to carbon monoxide of HT-PEMFC is higher than that for low temperature-PEMFC, the concentration of carbon monoxide in the syngas (stream 12) is much higher than the acceptable level for the anode of the fuel-cell stack (with a volumetric fraction range between 8 and 10% in the dry syngas). Therefore, a WGS reactor is placed after the heat-exchanger reactor, which not only decreases the amount of carbon monoxide via WGS reaction but also increases the hydrogen selectivity. After the energy recovery stage, the WGS reactor inlet temperature of approximately 530 °C (stream 12) is cooled down to about 280 °C. The WGS outlet (stream 13) is used for hot sanitary water generation in heat exchangers. The catalyst for high-temperature WGS reaction is composed of Fe_2O_3, Cr_2O_3, and MgO. The chromium acts to stabilize the iron oxide and prevents sintering. The granule-shaped catalysts operate in a temperature range of 310−450 °C. The water content is removed before entering the anodic side of the high-temperature proton exchange membrane stack, whereas, on the cathodic side, air is routed through ventilation to provide the required oxygen (stream 18). As a result, the electrochemical reaction is carried out by simultaneously producing electricity and useful heat. The anodic outlet (stream 17), which contains unreacted hydrogen and methane, is directed into the catalytic burner for the combustion reaction with auxiliary methane to generate the heat for the heat-exchanger reactor and for sanitary hot water (stream 28) after the thermal energy recovery stage in the exchangers (streams 26 and 27). In addition, the compressed air (stream 8) is fed into the burner (approximately 100 mbar) to provide the oxygen for catalytic combustion and to reach the desired temperature for the combustion exhaust. The useful heat produced by the stack is recovered by a TEG circulation unit (streams 33, 34, and 35) in order to supply the heat for preheating the demineralized water (stream 22), for the SMR (stream 23) and for sanitary hot water (stream 31).

Figure 4b presents the heat-exchanger reactor module created in the software dedicated to compact reactor modeling developed in ProSimPlus[36] with its inlet and outlet streams (details in Section 2.2). The fuel cell module (Figure 4c), the configuration of the stack simulation, and the model development are discussed in detail in Section 2.4.

Table 2 details the measured information of the important streams shown in Figure 4a. The experimental setup is equipped with pressure and temperature sensors, flowmeters, and valves for gas sampling. The measurements described here will be further compared with the results obtained from the simulation model.

Table 2. Measured Features of the Main Streams of the Experimental CHP System. Stream Numbers Refer to Figure 4a

stream	description	measurement performed
10	temperature of exhaust gas at burner inlet	$T_{exhaust\ inlet}$
11	temperature of exhaust gas at reformer outlet	$T_{exhaust\ outlet}$
7	temperature of syngas at reformer outlet	$T_{syngas\ outlet}$
13	outlet temperature of syngas at WGSR outlet	$T_{syngas\ out\ WGSR}$
2	process methane flowrate	$\dot{v}_{CH4\ Proc}$
7	molar fraction of syngas at reformer outlet	$x_{syngas\ SMR}$
13	molar fraction of syngas at WGSR outlet	$x_{syngas\ WGS}$

Pictures of the experimental setup are shown in Figure 5a. The important technical pieces of equipment are indicated with additional information in Table 3. The continuous gas analyzer "Siemens ULTRAMAT 23" used for the composition measurement of outlet syngas allows the continuous and simultaneous measurement of up to four gas components such as CO, CO_2, H_2, or CH_4. The instrument can be equipped with the infrared (IR) detector for IR active gases.

The upper operating range of the electrical power can reach up to 1.2 kW. A mechanical bleed resistor is integrated in the module, connected to the terminals of the cell. Its purpose is to ensure that the voltage of the fuel cell never exceeds a value close to 750 mV/cell. During operation, the load increase should be limited to 1 A/s. The fuel cell, a serenus 25/65/120 liquid C stack, was manufactured by SerEnergy and is made up of 50 cells with the objective to satisfy the power demand, and the entire stack assembly is installed in a cabinet. The power, communication, and cooling connections, as well as the process and cooling air inlets and outlets, are shown in Figure 5b. A module, called "power load," is installed, which continuously consumes the power generated by the stack: it allows an instantaneous measurement of the electrical power supplied by the stack.

The polarization curve obtained from the experimental campaign of the HT-PEM fuel cell will be compared with the fuel cell model, detailed in the following section. This curve is obtained as a data set in the form of (i; V_{cell}) couples that will be exploited for parametric model identification.

2.2. Heat-Exchanger Reactor and Corresponding Model. Figure 6 presents a simplified view of the compact millistructured heat-exchanger reactor, with schematic axial and longitudinal cross sections. The top part of this metallic additively manufactured module is composed of complex-shaped distribution and collection chambers that connect the reactants inlet, the products outlet, and the exhaust gas inlet and outlet to the millichannels. The distribution system is designed to allow co-current flow of burner exhaust gas and reforming products, while the reactants flow counter-currently: this flow configuration was chosen to improve internal heat integration and maximize methane conversion.

The core of the reactor consists of vertical parallel channels: 160 exhaust gas channels, 160 reactant channels, and 80 product channels. The reactor design creates channel layers, similar to the flow passages in plate-and-fins heat exchangers, so that the reactor can be decomposed into repetitive groups of channels containing 2 reactant channels, 2 exhaust gas channels, and 1 product channel (Figure 6, left). Details about reactor geometry is provided in Table 4. Only the reactant channels are coated with the catalyst.

The modeling of such a compact heat-exchanger reactor in CAPE-OPEN simulation software, such as ProsimPlus, can be performed by considering specific unit operations such as plate-and-fin heat exchangers and activating local reaction kinetics. The model assumptions for the multi-channel heat-exchanger reactor are based on the generic "common wall temperature" (CWT) assumption, enabling a general one-dimensional shape of the model. Two assumptions are considered for the wall temperature in this mode. The first assumes that the temperature of the reactor walls is homogeneous in its cross-section for similar channels (reactants, products, heating gas), i.e., along the x and y "radial" axes (Figure 7), and varies only along the longitudinal z axis ($T_{wash\ coat} = T_{wash\ coat\ surface} = T_{exchanger\ material}$). The second assumption considers that the
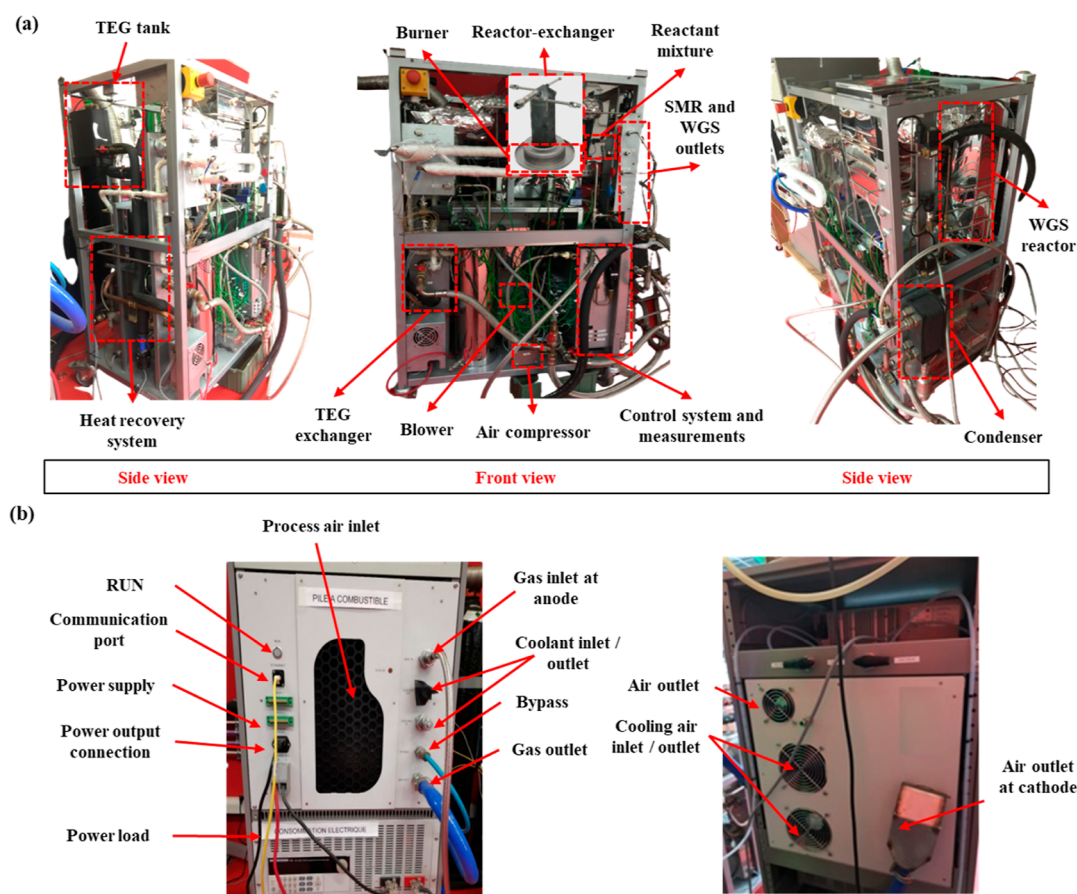
Figure 5. (a) Picture of the complete experimental setup of the micro-cogenerator pilot plant; (b) interface of the stack with the power, communication, and cooling connections.

Table 3. Information About the System Components

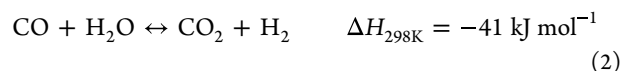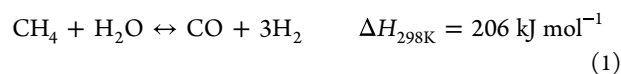| component	manufacturer	model/type
WGS reactor	AUER	flat plate reactor
condenser	Zilmet	28-plate heat exchanger
burner	Polidoro	metal fiber burners
air blower	HIBLOW Yasunaga	AP 100DU
metering pump	IWAKI	HRP54V 1P2 12V
gas compressor	HIBLOW	FC-2030-G

temperatures of all the layers of channels in the heat-exchanger assembly are identical at a given axial position z in the heat exchanger. This assumption is justified by the metallic mass of the reactor, which facilitates the thermal homogenization in the radial direction. These two assumptions can be justified by the fact that the thickness of the metal is relatively large, the effects of conduction in the metal are quite rapid compared to the effects of convection, the resistance to heat transfer by conduction is far negligible compared to the resistances by convection.

The model has been implemented in the CO-PROSEC reactive module, which is an operational unit dedicated to the simulation of multi-fluid plate-and-fin heat exchangers in the ProSimPlus v3.6.16 environment. The following assumptions have been adopted for the description of the model equations by representing the intensified catalytic heat-exchanger reactors.

- Steady state is considered.
- The flows are single-phase.
- The thermodynamics are continuous (i.e., not tabulated) for reactive fluids.

- The external mass transfer between the fluid phase and the catalyst is considered very rapid.[28]
- All the ducts in a given layer (reactants, products or heating gas) have the same behavior.
- The flow in channels is an ideal plug flow (no axial dispersion).[28]
- The radiative heat transfer is not considered.
- The fluids are Newtonian.
- The general gas equation is used for the CO-PROSEC; the Peng−Robinson's equation of state is used for the remaining system.

Two key reactions occur in the reactive channels

$$CH_4 + H_2O \leftrightarrow CO + 3H_2 \qquad \Delta H_{298K} = 206 \text{ kJ mol}^{-1} \tag{1}$$

$$CO + H_2O \leftrightarrow CO_2 + H_2 \qquad \Delta H_{298K} = -41 \text{ kJ mol}^{-1} \tag{2}$$

The first reaction (SMR) is considered to be a pseudo-homogeneous reaction modeled with reaction kinetics. This assumption can be justified by the fact that CO-PROSEC considers that the limitations to the external mass transfer are negligible, in accordance with the results of the literature.[37] The rate law (eq 3), used in the CO-PROSEC reactive module for the SMR reaction, is based on the kinetic law developed in the work of Mbodji et al.[28,38]
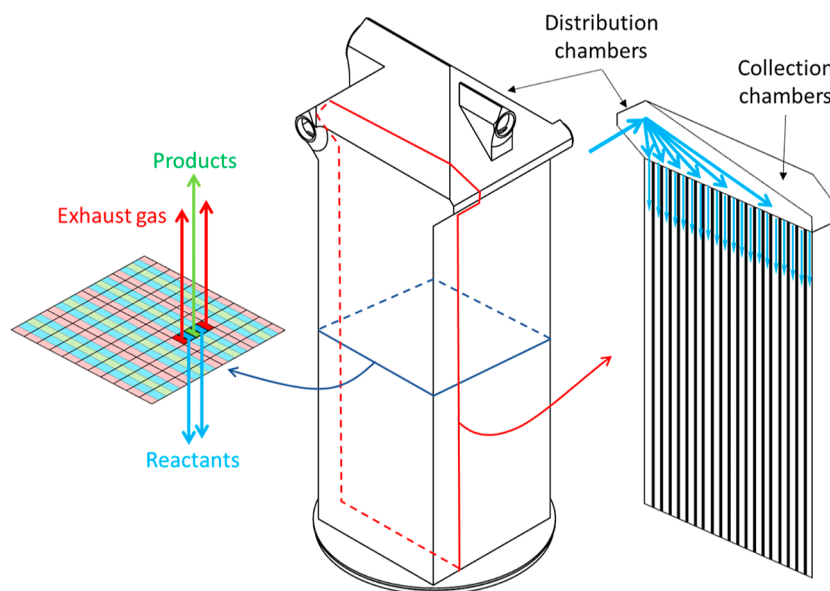
Figure 6. Schematic design of the experimental SMR reactor, with horizontal cross section (left) and longitudinal cross section (right).

Table 4. Description of the Geometry of the Reactor-Exchanger

	reactive fluid flow data	syngas passage data	exhaust gas flow data
equivalent channel section	circular	circular	circular
equivalent channel diameters (mm)	3.6	2.0	1.7
number of passages	8	4	8
total number of channels	160	80	160
exchange length (mm)		179.3	
reactions	SMR and WGS	no	no
material of the exchanger		Inconel 625	

$$R_{SMR} = K_\mu \cdot \frac{P_m}{\Omega} \cdot A_{SMR} \cdot \exp\left(-\frac{E_a^{SMR}}{R \cdot T^s}\right) \cdot$$

$$\left(P_{CH_4} \cdot P_{H_2O} - \frac{P_{H_2}^3 \cdot P_{CO}}{K_{eq}^{SMR}}\right) \tag{3}$$

In eq 3, P_m represents the wetted perimeter of a channel, Ω is the fluid flow cross section, A_{SMR} is the pre-exponential factor of the SMR, which is equal to 2.14×10^5 mol m$_{ams}^{-2}$ s^{-1} bar^{-2}, E_a^{SMR} is the activation energy of the SMR reaction, and P_i is the partial pressure of species i. The microstructure constant K_μ is determined in the thesis work of Mbodji et al.[28,38] and is a function of the properties of the catalyst expressed by eq 4, which is equal to 666 m$_{ams}^2$ m$_{catalyst}^{-2}$

$$K_\mu = A_m \cdot M_c \cdot PR \tag{4}$$

In eq 4, A_m is the surface of active metal per mass of active metal (ams), M_c is the mass of catalyst deposited per unit of projected surface of the wash-coat, and PR is the active metal content of the catalyst. The reactive micro-channels of the heat-exchanger reactor are coated with a catalyst wash-coat (1% Rh/MgO−Al$_2$O$_3$), the temperature of calcination is 450 °C, the specific metal surface is 369 m^2 g$_{metal}^{-1}$, the surface mass is 180 g m$_{wall}^{-2}$, and the deposit thickness is 100 μm.

The WGS reaction cannot be neglected, although it is thermodynamically disadvantaged at the temperatures studied. This reaction is rapid enough to be considered at thermodynamic equilibrium at any point along the reactive channels. This simplification is useful to perform rapid parametric studies within a reasonable range of operating conditions and reactor-exchanger geometries. The range of steam-to-methane ratio in the reactor feed is 3−4.5.

The thermodynamic equilibrium constants for the SMR and WGS reactions can be expressed as[28]
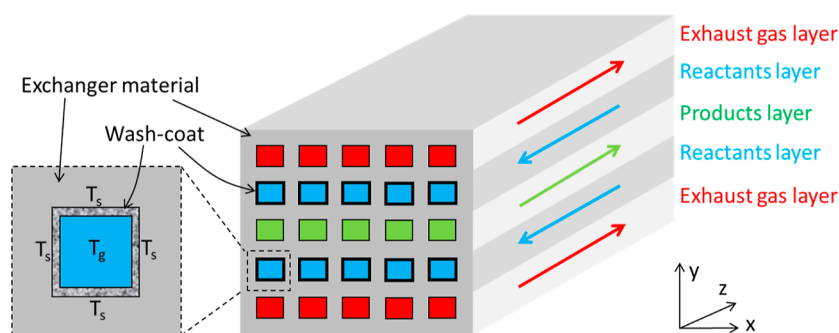

Figure 7. Cross-sectional view of the various flow layers in the heat-exchanger reactor, with temperatures in the catalytic channels (wash-coat) according to the "CWT" assumption. Ts: temperature of the wall, the catalyst, and the surface of the catalyst.

$$K_{eq}^{SMR} = \exp\left(-\frac{26,830}{T} + 30.114\right) [bar^2] \qquad (5)$$

$$K_{eq}^{WGS} = \exp\left(\frac{4400}{T} - 4.036\right)[—] \qquad (6)$$

In order to validate the integration of the CO-PROSEC reactive module in the complete simulation of the micro-CHP process based on a HT-PEM fuel cell, the main information to be defined includes (i) parameters: thermal conductivity of the material, dimensions of the reactor-exchanger body, numerical parameters, etc.; (ii) streams: hot sources, cold sources, reactants, chemical reactions, recycling, etc.; (iii) channel geometries: hydraulic diameter, plate thickness, etc.; and (iv) reference passages: passages and blocks, stacking, elementary areas (synthetic views), etc. The data provided in Table 4 are translated into the CO-PROSEC reactive formalism. Additional details and benchmark studies of this specific modules are provided in dedicated ref 39.

2.3. Water Gas Shift Reactor. The WGS reactor is a fixed-bed-type reactor, with heat management to ensure that the reaction temperature is maintained in the active range of the used catalyst (<300 °C). A plate-type geometry is used to improve heat transfer between the catalytic particles, which exhibit a low thermal conductivity, and the heating hot gases coming from the SMR reactor. This planar geometry provides a large heat-exchange area and the small thickness of the heat-exchange plate allows to accelerate heat transfer by decreasing the thermal diffusion time. The heating side contains baffles to force the hot gas to follow a serpentine-shaped trajectory to still enhance heat-transfer coefficients. The temperatures of both fluids are measured at the top (inlets) and bottom (outlets) of the reactor, and the reactor is insulated to avoid loss of efficiency.

Under the studied operating conditions, preliminary experiments confirmed that the WGS reaction is fast compared to the reactants space time and that the output mixture has reached thermodynamic equilibrium at the outlet temperature. The WGS reactor, is therefore, modeled as a Gibbs reactor considering the stoichiometry and species described in the previous section. Depending on the aim of the simulation, different specifications are considered for this Gibbs reactor: an output temperature specification is used for comparison of the output mixture composition with experimental values for validation through experimental campaigns, whereas a heat duty specification is used, with regulation of the outlet temperature below 300 °C, for simulation and process integration.

2.4. HT-PEMFC Stack Module and Selected Model. The elementary fuel cell is a stack of four main parts: bipolar plates, diffusion layers, catalytic layers, and membrane. In the center of the cell is the electrolyte, including a polymer membrane. The electrodes, together with the membrane and catalytic layers, constitute the membrane electrode assembly (MEA), where the oxidation of hydrogen and reduction of oxygen occur and produce water and electricity. At the extremities of the cell are the electron-conducting bipolar plates where the anode and cathode gas distribution channels are carved. Additionally, the stack includes the pre-heater and coolant circuit, where the reactants (syngas and air) exchange heat with the circulating coolant (TEG) to attain the desired temperature.

In this work, two models of HT-PEMFC have been studied: the former is a physics-based theoretical model, and the latter is a correlative mathematical model. Indeed, two different modeling approaches, either based on theory (white-box approach) or on a purely mathematical approach (black-box approach), can be considered to represent the polarization curve obtained from the experiments. The objective is different for the creation of the two models: the theoretical model allows the adjustment of the operating current density of the HT-PEMFC stack to meet various load requirements, including summer cooling and winter heating modes, whereas the mathematical model simplifies implementation in the ProSimPlus v3.6.16 simulation software for the calculation of the current density, voltage, and methane inlet flow rate for the reforming reaction as a function of the required power. It is useful to recall that the experimental determination of the polarization curve provided a data set in the form of $(i; V_{cell})$ couples that can be exploited for parametric model identification.

For concision, only the mathematical model is detailed here. For interested readers, the physics-based model is presented in the appendix. The expression of the mathematical model is described by eq 7

$$V_{cell} = a_6 + a_7 \times i + a_8 \times i^2 + a_9 \times i^3 \qquad (7)$$

The values of the coefficients a_6 to a_9 are obtained in Matlab by conventional multiple linear regression, applied to the experimental data of the polarization curve. Their values and the 95% confidence intervals are provided in Table 5: the very

Table 5. Values of the Coefficients of the Mathematical Model and Their 95% Confidence Intervals

coefficient	value
a_6	0.75 ± 0.00170
a_7	-2.47 ± 0.0547
a_8	11.21 ± 0.467
a_9	-20.99 ± 1.129

narrow confidence intervals confirm the strength and reliability of this correlative model over the range of experimental measurements ($i_{exp} = 0.021-0.25$ A cm^{-2}). Figure 8 compares the experimental data and the two models: the simplified polynomial model exhibits the same quality as the physics-based
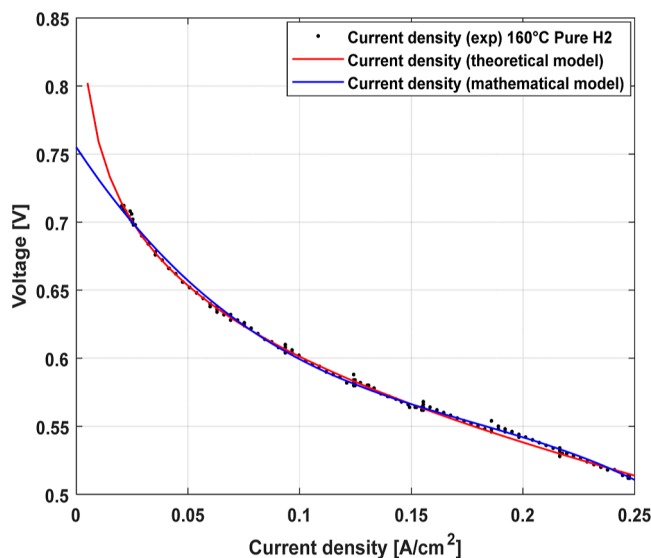

Figure 8. Validation of the mathematical model for the HT-PEM fuel cell.
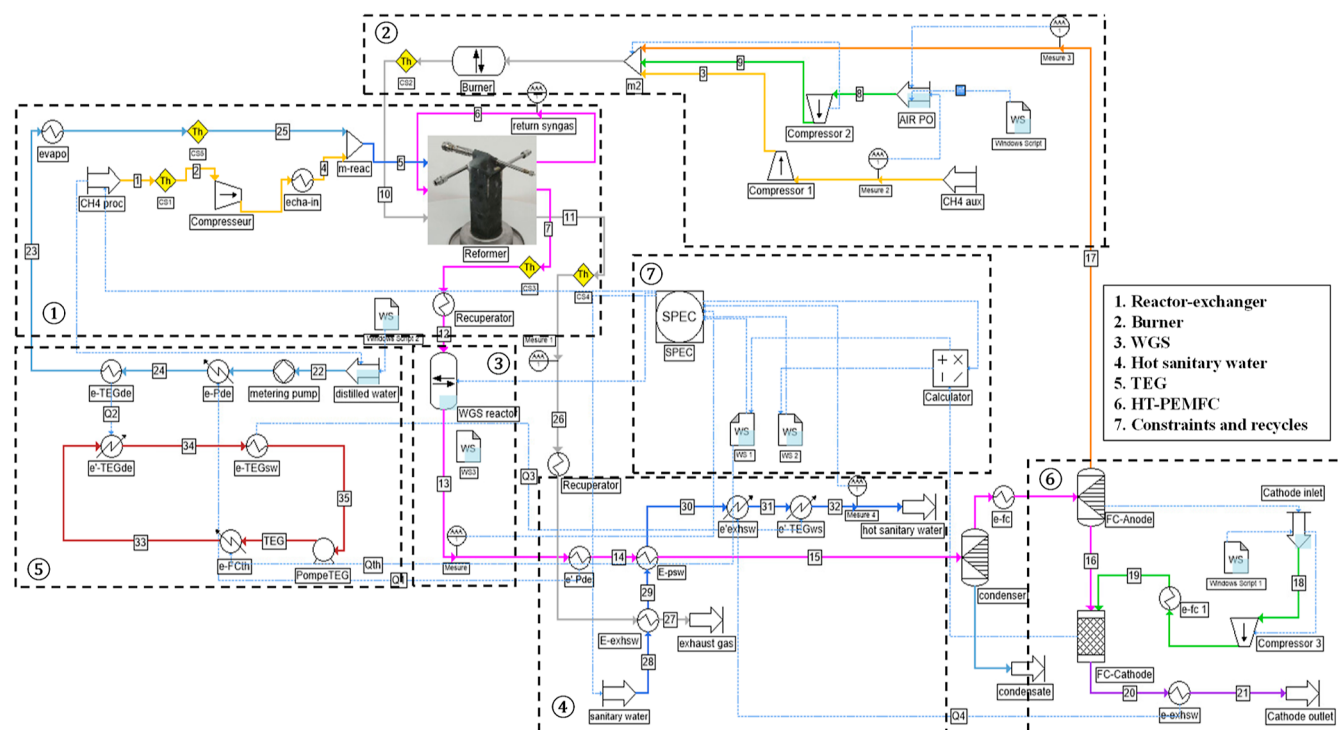
Figure 9. Simulation of the complete process in ProsimPlus.

Table 6. Specification and Variable Definitions in Module SPEC

$N°$	specification	description	adjusted variables	lower bound	upper bound
1	P_{el}	electrical generation	process CH_4 flow rate (kmol h^{-1})	8.0×10^{-4}	1.6×10^{-2}
2	T_1	outlet temperature at WGS reactor	Q_{th} (kcal h^{-1})	-60	-40
3	T_2	outlet temperature of hot sanitary water	hot sanitary water flow rate (kmol h^{-1})	3	8
4	η_{el}	electrical efficiency	η_{el} (—)	0.35	0.70
5	x_{H_2}	hydrogen molar fraction in syngas	auxiliary CH_4 flow rate (kmol h^{-1})	2.8×10^{-5}	2.4×10^{-2}

theoretical model in representing the system over the range of experimental conditions. However, as soon as the operating range is extrapolated, especially at a low current density, the polynomial model starts to deviate rapidly and no longer represents the system reliably. Although this black-box model is limited, it is easier to use in ProSimPlus than the previous approach: particular attention should be paid to its application if extrapolated conditions are studied. The polarization curve of the fuel cell obtained from the mathematical model has, therefore, been retained and implemented in the complete simulation model. Its integration in a set of unit operations is described in the next section.

2.5. Process Plant Simulation and Specifications. Figure 9 presents the complete process simulation developed in ProsimPlus, a process engineering software that performs rigorous steady-state mass and energy balances for a wide range of industrial processing plants. The streams presented in this figure correspond to the same streams as shown in Figure 4a. In the following sections, the presentation of the results obtained from the model will be based on the configuration presented in this figure. The unit operations are framed by different blocks to highlight each zone of the process.

1. The heat-exchanger-reactor: as detailed in Section 2.2, this compact unit is modeled by analogy to a plate-and-fin heat exchanger, including catalytic reactions in the reactant's channels thanks to the CO PROSEC reactive

module. All compressors in the simulation are specified with a fixed outlet pressure of 120 kPa, an isentropic efficiency of 70%, and ideal mechanical and electrical efficiencies.

2. The catalytic burner is modeled as an equilibrium Gibbs reactor at a specified temperature of 850 °C.

3. The WGS reactor: as indicated in Section 2.3, the WGS reactor is modeled as a Gibbs reactor.

4. The production of sanitary hot water is composed of a set of heat exchangers integrating the flow of sanitary water to the hot exhaust gases of the heat-exchanger reactor, WGS reactor, fuel cell and to the TEG loop.

5. The TEG loop, in addition to integration heat exchangers, contains a pump, specified with an output pressure of 120 kPa and an efficiency equal to 70%.

6. The fuel cell stack: after flowing through an ideal condenser that separates excess water from the WGS output, an ideal separator splits the inlet stream according to a ratio calculated on the basis of the anode stoichiometry. The cathode is modeled as a full conversion reaction considering the hydrogen oxidation stoichiometry at a temperature of 160 °C.

7. The constraints and recycles are managed by the SPEC unit: the mathematical model of the polarization curve is incorporated into the process simulation as a user-defined function (Windows Script).

Table 7. Outlet Dry Molar Fractions of Reformer and WGS Reactors Obtained from the Model and the Experimental Data (n.c.: Not Computable)

test				$N°1$				$N°2$				$N°3$
CH$_4$ process flow rate $\dot{v}_{Stream2}$ (L min^{-1})				2				3.5				4
temperature exhaust inlet $T_{Stream10}$ (experiment, °C)				795				856				873
temperature exhaust inlet $T_{Stream10}$ (model, °C)				800				865				880
temperature exhaust outlet $T_{Stream11}$ (experiment, °C)				443				465				470
temperature exhaust outlet $T_{Stream11}$ (model, °C)				474				499				502
temperature syngas outlet $T_{Stream7}$ (experimental, °C)				348				380				385
temperature syngas outlet $T_{Stream7}$ (model, °C)				431				456				460
temperature bottom WGS reactor T_{shift} (experiment, °C)				234				243				268
WGS outlet temperature $T_{Stream13}$ (model, °C)				130				176				190

test	$N°1$				$N°2$				$N°3$			
dry molar fraction (%)	CH$_4$	H$_2$	CO	CO$_2$	CH$_4$	H$_2$	CO	CO$_2$	CH$_4$	H$_2$	CO	CO$_2$
SMR outlet, stream 7 (experiment)	3.46	75.57	8.72	12.25	2.28	75.88	11.51	10.34	1.86	76.19	11.62	10.33
SMR outlet, stream 7 (model)	3.94	75.06	8.89	12.11	1.89	76.31	10.86	10.94	1.81	76.32	11.13	10.74
relative error (%)	12.18	0.68	1.91	1.16	20.63	0.56	5.99	5.48	2.76	0.17	4.40	3.82
WGS outlet, stream 13 (experiment)	3.42	77.26	<0.01	19.32	1.70	78.64	<0.01	19.66	0.97	79.23	<0.01	19.81
WGS outlet, stream 13 (model)	3.17	77.55	0.01	19.27	2.05	78.34	0.06	19.55	1.54	78.75	0.08	19.63
relative error (%)	7.89	0.37	n. c	0.26	17.07	0.38	n. c	0.56	37.01	0.61	n. c	0.92

In the present work, the electrical production of the system is considered to be 1 kW, which is a system specification: the system is designed to satisfy the energy and thermal regulations for a proportional part of the energy demand of new individual buildings. The system is assumed to be grid connected to ensure the balance between energy consumption and distribution.

All unit operations are linked by the central module of constraints and recycles (SPEC) through information streams, represented by the blue dotted lines. This central module enables us to solve the equations between the specifications and the setpoints by adjusting the action variables. The variables are defined in the process simulation depending on the studied cases, and their bounded values are shown in Table 6. For improved convergence, teared streams are initialized according to the results of a previously converged simulation. The Newton−Raphson numerical scheme is used for teared streams and specifications.

2.6. Heat-Recovery System. A heat-recovery system is used to collect excess heat from the outlet streams of the heat-exchanger reactor and the available thermal energy of the fuel cell.

Two recuperators are employed to recover the thermal heat of syngas and off-gas, respectively, at the outlets of the SMR reactor. At steady state, the useful heat of syngas is recovered as the heating resource for superheated steam and process fuel. Based on a local pinch analysis, to maintain the existing structure of the system, the current optimal solution consists in adding two exchangers at the syngas outlet to enable the heat transfer between the products and the process input fuel in a first step and then with the steam being preheated by the TEG loop. On the exhaust gases side, the hot off-gas is used to preheat the air at the stack inlet, then an additional cooler provides cold utility to the system. The syngas and exhaust gases are then directed to the heating of sanitary water before being conducted into the anode and evacuated respectively.

Concerning the heat generated in the fuel cell, during steady-state operation, it is evacuated by the TEG loop, which includes a pump, a filter, a tank, and two exchangers connected to the demineralized water and sanitary water circuits, respectively.

2.7. Performance Indices. The indices used for the evaluation of the performance of the fuel cell-based micro-

CHP system are defined in the present section before discussion of the results. Four performance indices are considered: the net electrical efficiency ($\eta_{net\ el}$), the gross electrical efficiency ($\eta_{gross\ el}$), the thermal efficiency (η_{th}), and the overall efficiency (η_{total}).

The net electrical efficiency is defined as the ratio between the net electricity generated by the stack, which excludes the use of auxiliary energy (BOP), and the chemical energy of the fuel input to the system

$$\eta_{net\ el} = \frac{P_{gross\ el} - \sum_i BOP}{\dot{n}_{CH_4}^{tot} \times LHV\ CH_4} \tag{8}$$

The balance of plant (BOP) includes the energy required by the four compressors and two pumps that induce the flow of methane and demineralized water to the SMR unit, air and methane to the burner, air to the fuel cell, and TEG in the utility loop.

The gross electrical efficiency is obtained from the electrical power generated in the stack and the chemical energy input to the system

$$\eta_{gross\ el} = \frac{P_{gross\ el}}{\dot{n}_{CH_4}^{tot} \times LHV\ CH_4} \tag{9}$$

The thermal efficiency is defined as the useful heat ($Q_{th\ total}$), which includes the thermal power generated by the stack (Q_{th}) and that recovered by sanitary water ($Q_{th\ sw}$), divided by the chemical energy input to the system

$$\eta_{th} = \frac{Q_{th} + Q_{th\ sw}}{\dot{n}_{CH_4}^{tot} \times LHV\ CH_4} \tag{10}$$

Accordingly, the overall efficiency of the system is defined as the sum of the net power output and the recovered useful heat divided by the chemical energy input to the system

$$\eta_{total} = \frac{P_{net\ el} - Q_{th} + Q_{th\ sw}}{\dot{n}_{CH_4}^{tot} \times LHV\ CH_4} \tag{11}$$

The reforming factor is used to determine the performance of the fuel processor; it is defined as the total energy generated by
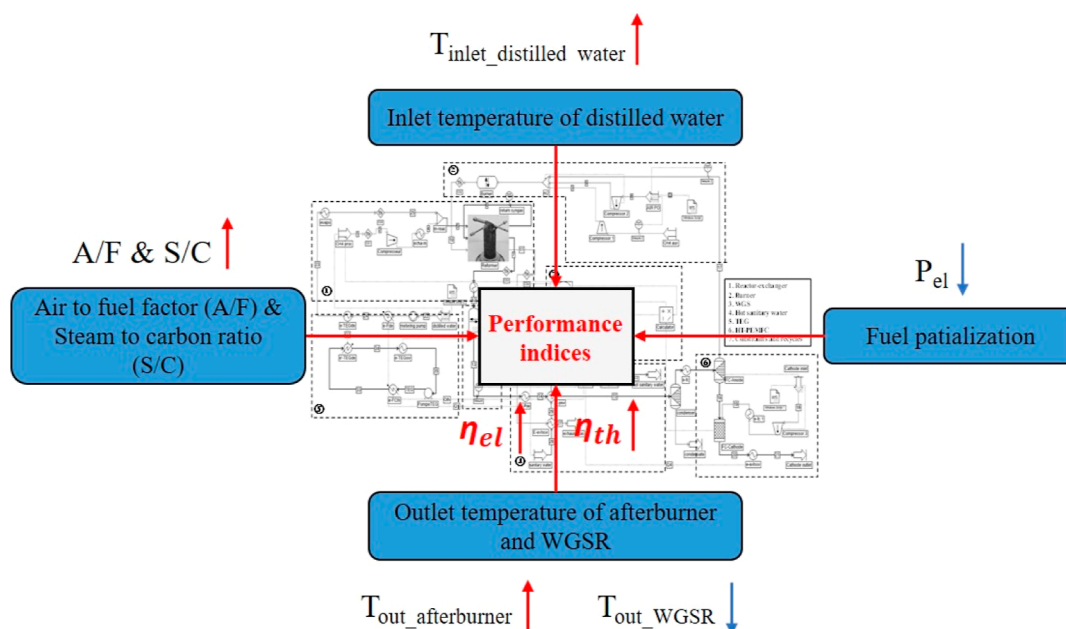
Figure 10. Schematic view of the sensitive parameters on performance indices.

hydrogen in the anodic inlet divided by the total chemical energy input to the system

$$\mathrm{RF} = \frac{\dot{n}_{H_2}^{\mathrm{anode\text{-}in}} \times \mathrm{LHV\ H_2}}{\dot{n}_{CH_4}^{\mathrm{tot}} \times \mathrm{LHV\ CH_4}} \qquad (12)$$

3. RESULTS AND DISCUSSION

The following sections will first enable us to validate the simulation tool on the basis of a comparison with experimental data from the CHP plant and then to explore a larger range of possible operating conditions, through simulation, to search for maximal thermal and electric efficiencies of the plant, according to fuel partialization or full-load operation. The flexibility of this highly integrated system will be assessed stepwise. A pinch analysis of the complete plant will finally be proposed to further increase process efficiencies.

3.1. Model Validation of the Fuel-Reforming Processor. The validation of the fuel processor model was carried out by comparison with the experimental setup under various operating conditions corresponding to increasing process flow rates. The behavior of the fuel-reforming processor was studied by measuring the syngas compositions at the outlet of the reformer and WGS reactor units. The compositions of the syngas at the outlet were determined using a continuous gas analyzer. Three experimental tests, with increasing process methane flow rates, have been carried out at 2, 3, and 4 L min^{-1}.

The dry gas compositions predicted by the simulation at the outlets of the heat-exchanger reactor and WGS reactor are compared with the experimental data in Table 7. The syngas temperatures at the outlet of the reformer and WGS reactor from the model and experiments are presented in Table 7. The largest and smallest possible measuring ranges are respectively used for CO_2, CH_4, and CO molar fractions. The errors in the largest and smallest ranges are less than ± 1 and 2%, respectively, of the full-scale value.[40]

Three different tests, with increasing process methane flow rates, are compared: the outlet molar fractions of the dry gas only exhibit a subtle difference between the experimental and the

model data. The model predicts the experimental reformer performance with good accuracy.

Although some discrepancies exist between the measured and calculated values, which will be explained below, the model predicts quite well the effects of the increased methane flow rate on the outlet gas reformer temperatures. Concerning the inlet temperature of hot exhaust gas, no significant differences between the model and experiments are observed, by opposition to the outlet temperatures that exhibit significant gaps. The reason for such differences between the modeled and experimental outlet temperatures lies in the location of the measurement probe that was not positioned exactly at the point where the outlet streams are located, inducing impact of heat losses that are difficult to estimate. In addition, the syngas product flow rate is much lower than the exhaust gas flow rate, and the measurement probe is located closer to the inlet of the WGS reactor than to the reformer outlet, so that the outlet temperature of the syngas presents higher discrepancy with the modeled temperature than with the exhaust gas outlet temperature.

The experimental temperatures of the WGS reactor presented in Table 7 are the temperatures measured in the lower part of the WGS reactor, and those of the model are the temperatures of the syngas, which comes out of the WGS reactor. Before entering the gas analyzer, the syngas may have been affected by a slight catalytic effect of the tube material, which means the reaction has continued in the duct. The dry mole fractions of the syngas are close to those corresponding to the syngas outlet temperature; therefore, the syngas outlet temperature has been taken as the reference temperature to validate the simulation of the WGS reactor.

The obtained dry fractions at the SMR and WGS outlets have been compared with the experimental data, and the relative error has been calculated. Even though the error is relatively large between the experimental and modeled data for CH_4, the model predicts the fractions of CO and H_2 with a good accuracy.

3.2. Sensitivity Study of Fuel Partialization Approach. This section presents the results of the sensitivity analysis for the complete process simulation. The performance and flexibility of

the highly integrated system under the fuel partialization strategy is studied, and the electrical and thermal efficiencies of the fuel process under different partial fuel conditions are determined. The fuel partialization is performed by varying the fuel flow rate: a large range is chosen to assess the evolution and the limitations of the system efficiencies. According to Arsalis et al.,[41] it should be noted that if the stack is continuously operated at a part-load below 25%, the higher selected nominal cell voltage does not necessarily induce a higher operating efficiency. This is due to operation at very low current densities, where parasitic losses, including gas permeation through the polymer membrane, may not be negligible. A summary of the sensitive parameters is given in Figure 10.

3.2.1. Evolution of Electrical and Thermal Production. The first step consists in gradually reducing the molar flow rate of the supplied fuel and then monitoring the system performance under different fuel partialization conditions. The operating parameters are given in Table 8.

Table 8. Operating Parameters of the HT-PEMFC Based CHP Plant

operating parameter	value
steam-to-carbon ratio (S/C)	3.5
air-to-fuel (A/F) ratio [r_1, r_2]	[30, 7.5]
combustor outlet temperature (°C)	850
temperature of WGS reactor (°C)	300
inlet temperature of distilled water (°C)	191
inlet temperature of process methane (°C)	400
temperature of reactants mixture (°C)	253
anodic stoichiometric ratio	1.35
cathodic stoichiometric ratio	2.5
fuel cell operating temperature (°C)	160

The air-to-fuel (A/F) ratio describes the relation between the requirement of air and fuel in the burner and, therefore, incorporates two ratios for the molar flow rate of the auxiliary methane (r_1) and for the exhaust of the anode (r_2), respectively

$$\dot{n}_{Air}^{Burner} = \dot{n}_{CH_4}^{aux} \cdot r_1 + \dot{n}_{Anode}^{exhaust} \cdot r_2 \qquad (13)$$

The evolution of electrical and thermal production with the reduction of the inlet fuel from its initial value (100% corresponding approximately to an electrical generation of 1 kW) down to 7.3%, which corresponds to an electrical generation close to 100 W for the micro-CHP system, is shown in Figure 11. It can be observed that the electrical and thermal production logically decreases while the fuel input is reduced. The electrical generation decreases from 1018 to 113.2 W, and the thermal generation is reduced from 1445 to 86.3 W. While operating in the fuel-partialization mode, the power output of the micro-cogenerator can be modulated by changing the fuel supply. The use of the compact heat-exchanger reactor does not limit the range of operation regimes from lower to higher power generation. According to the needs of the residents as seasons change, fuel partialization gives the possibility to choose the most suitable operating mode.

3.2.2. Evolution of Electrical and Thermal Efficiencies. The same analysis with inlet fuel partialization is applied for the electrical and thermal efficiency, as shown in Figure 12a. Both efficiencies increase with the decrease of fuel partialization. The gain in the electrical efficiency can be explained with two main arguments: first, during low-power operation of the fuel cell, the
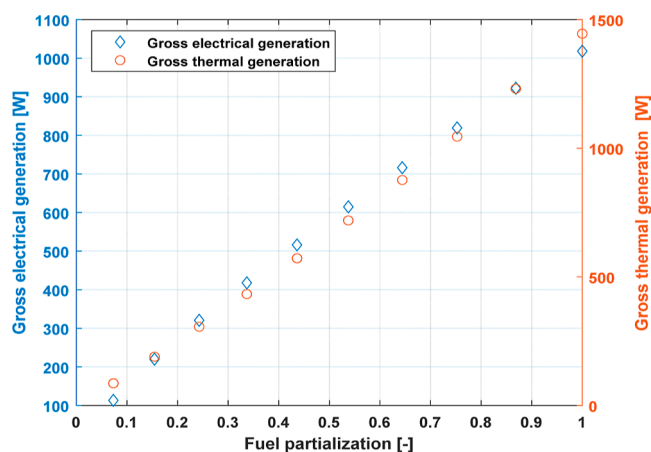

Figure 11. Evolution of electrical and thermal generation as a function of fuel partialization.
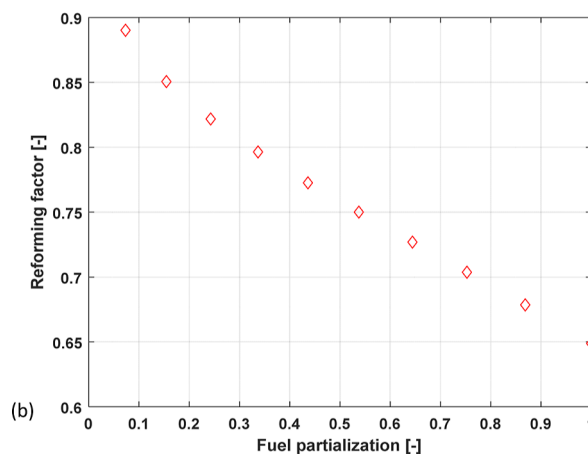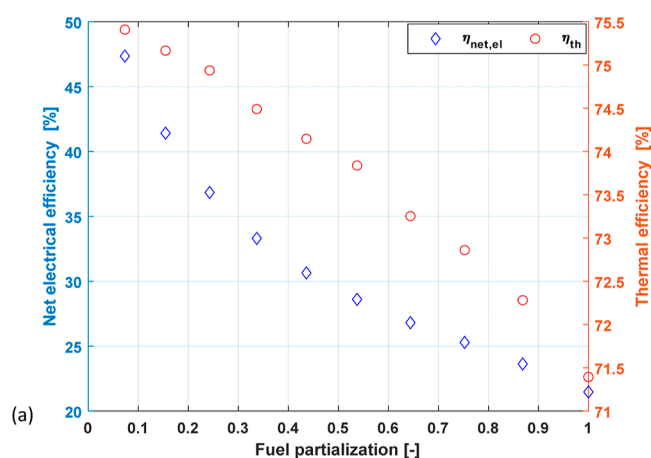

Figure 12. (a) Evolution of electrical and thermal efficiencies with fuel partialization and (b) evolution of the reforming factor with fuel partialization.

voltage losses are lower compared to high-power operation. Second, the demand of the process methane is lower at low power than at high-power operation, which enhances the reaction of steam reforming in the reformer. The latter is demonstrated by Figure 12b. The reforming factor increases when fuel partialization is decreased: since less hydrogen is provided, while maintaining the same operating conditions in the fuel cell, the current densities are reduced. Lower current

densities correspond to lower voltage losses, which results in a higher electrical efficiency at low-power operation. The thermal efficiency evolves regularly, presenting no saturation that could result from a pinch limitation of the integration heat-exchanger network or from the compact heat-exchanger reactor itself: flexibility is not constrained by heat integration.

3.3. Sensitivity Analysis of Full-Load Operation. In a second time, a sensitivity analysis is performed to evaluate the impact of different fuel-reforming processor operating conditions on the system performance. The combined effects of the steam-to-carbon (S/C) ratio and the air-to-auxiliary-fuel (A/F) factor are first discussed. The effect of the inlet temperature of distilled water is then investigated. Finally, the influences of the outlet temperatures of the afterburner and WGS reactor are studied.

3.3.1. Combined Impact of the S/C Ratio and A/F Factor. Table 9 presents the operating conditions of this step of the

Table 9. Operating Conditions of the HT-PEMFC-Based CHP Plant

operating condition	value
electrical power output (W)	1000
combustor outlet temperature (°C)	850
inlet temperature of distilled water (°C)	191
outlet temperature of WGS reactor (°C)	300
auxiliary methane flow rates	constant

analysis: the auxiliary methane flow rate is considered as a constant for each case at a given air-to-fuel factor, managed by the SPEC module.

As demonstrated in Figure 13a,b, the investigation has been carried out for different steam-to-carbon ratios (2−4.5) and air-to-fuel factors (25−30, 6.25−7.5). As can be seen in Figure 13a, increasing the steam-to-carbon ratio enhances the reforming factor: the higher the S/C value, the higher the steam reforming reaction rates and the hydrogen production. Moreover, increasing the air-to-fuel factor leads to a significantly reduced consumption of auxiliary methane and the highest reforming factor.

Figure 13b shows the combined effect on the conversion of process methane. On one hand, the air-to-fuel factor has almost no impact on the methane conversion. On the other hand, by modifying the S/C ratio, more than 98% conversion is attained at high S/C ratios. In addition, the achievement of high conversions directly demonstrates the intrinsic capacity of the heat-exchanger reactor and justifies the suitability of this compact unit in the micro-cogeneration system.

The effects of different S/C ratios and A/F factors on the net electrical efficiency have been studied and presented in Figure 14a. As explained previously, increasing the S/C ratio for fixed inlet operating conditions leads to a higher SMR rate, higher hydrogen production, and lower consumption of process fuel. Besides, enhancing the A/F ratio significantly reduces the consumption of auxiliary methane. Even though the net electrical efficiency is directly related to the reforming factor, the performance of the fuel cell has also an influence on the latter. Therefore, the electrical efficiency does not behave exactly the same way as the reforming factor.

A gradual decline in the increase of the electrical efficiency is noted by enhancing the S/C ratio, given that higher S/C ratios imply the requirement of higher steam flow rates, which in turn results in higher energy consumption in the vaporizer.
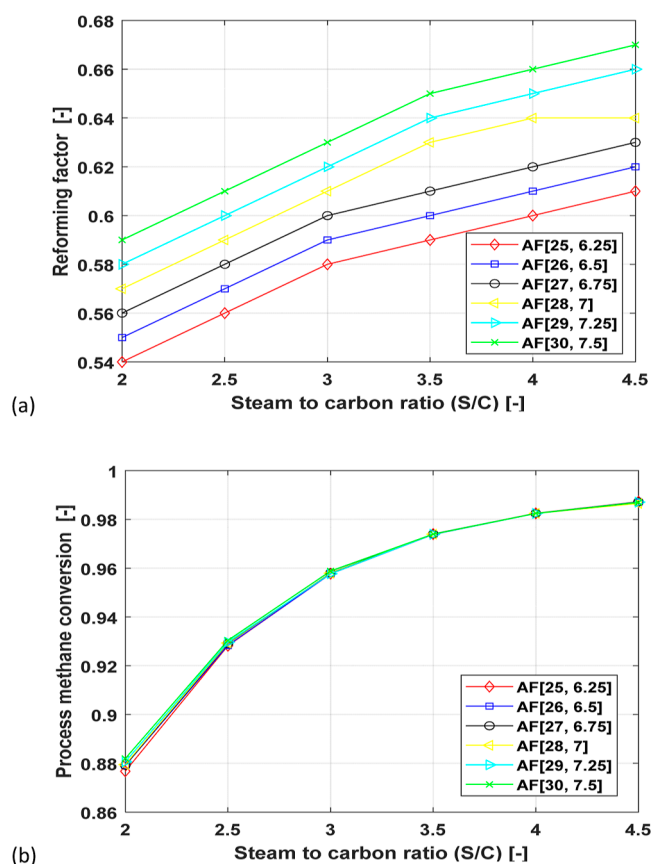

(a)

(b)

Figure 13. (a) Effects of the A/F and S/C ratios on the reforming factor and (b) effects of the A/F and S/C ratios on process methane conversion.

Otherwise, if no additional energy is provided to heat up the steam, the flow enters the reformer with a lower temperature, which leads to a decrease in fuel conversion. Moreover, although a higher A/F factor helps in reducing the demand of auxiliary methane, a larger air flow rate requires more sensible heat in order to maintain a correct combustion and the outlet temperature of the afterburner. It is noteworthy to choose a reasonable range of A/F factor values by considering, as well, the sensitivity of the heat exchange behavior in the heat-exchanger reactor.

The overlapping curves in the upper part of Figure 14b represent the molar fractions of CO in the dry syngas at the reformer outlet, and those at the bottom represent those at the anode inlet. Increasing the S/C ratio not only impacts the SMR reaction but also improves the rate of the WGS reaction that takes place in the reformer. Enhancing the SMR rate increases the production of carbon monoxide, whereas increasing the WGS reaction leads to a considerable decrease in this component. The effect of the S/C ratio on the WGS reaction is predominant, and the mole fraction of carbon monoxide decreases with increasing S/C ratio. It can also be seen that increasing the A/F factor has no impact on the performance of the considered reactions but has a great influence on the auxiliary methane flow rate and the efficiencies of the system.

The same effects are noticed at the anode inlet: the CO content is considerably reduced by operating the WGS reactor with an outlet temperature of 300 °C. This effect will be discussed further.
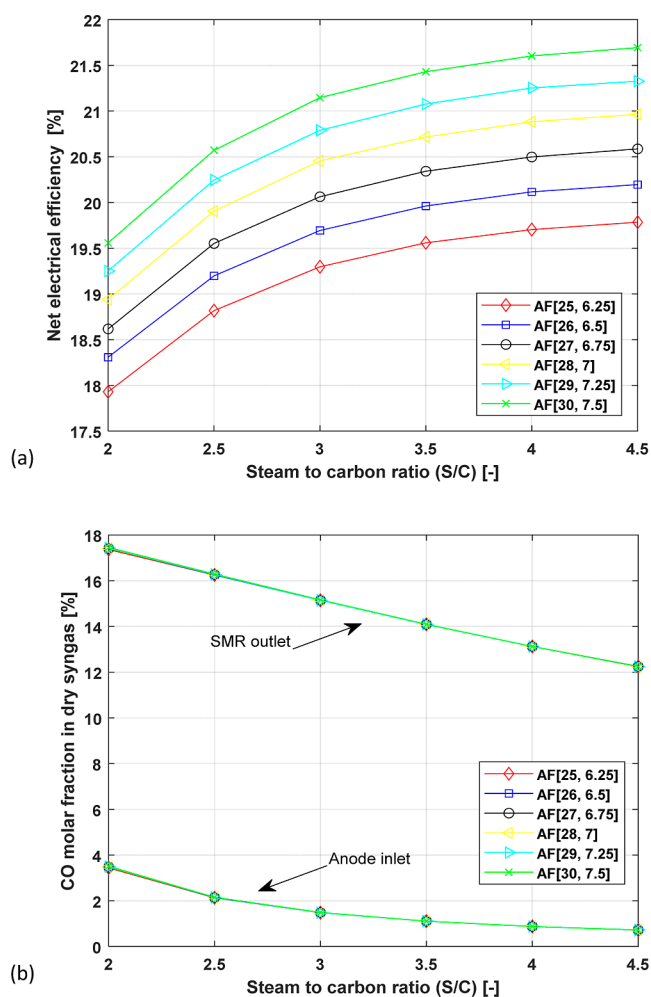
(a)

(b)

Figure 14. (a) Effects of the A/F and S/C ratios on the net electrical efficiency; (b) Effects of the A/F and S/C ratios on the CO molar fraction in dry syngas.

As a result, the highest values of electrical efficiency and reforming factor are obtained in the upper right zone (Figure 14a), so that the optimum conditions correspond to a large A/F ratio [30, 7.5]. For the remaining sensitivity analysis, a value of S/C equal to 3.5 will be selected, since the increase of the performance index slows down above this value, and a considerable generation of superheated steam requires a higher energy consumption.

3.3.2. Inlet Temperature of Distilled Water. The effect of the inlet temperature of distilled steam on the system efficiencies is investigated from 137 up to 400 °C ($T_{superheated\ steam}$). By setting the process methane temperature at 400 °C, the temperature of the reactant mixture varies from 215 to 400 °C ($T_{reactant\ in}$). Figure 15 shows that increasing the inlet hot steam temperature leads to only a small improvement of the electrical and overall efficiencies, despite a higher heat amount supplied for superheated steam. The electrical and thermal efficiencies slightly increase: this can be explained by the increased reactant temperature, which requires lower sensible heat to preheat the reactant mixture in the reactor with a given A/F factor value, thus reducing the consumption of the auxiliary methane. However, this effect of increased inlet temperature on the system efficiencies is not significant.

3.3.3. Outlet Temperature of Afterburner and WGS Reactor. The effects of the outlet temperature of the afterburner
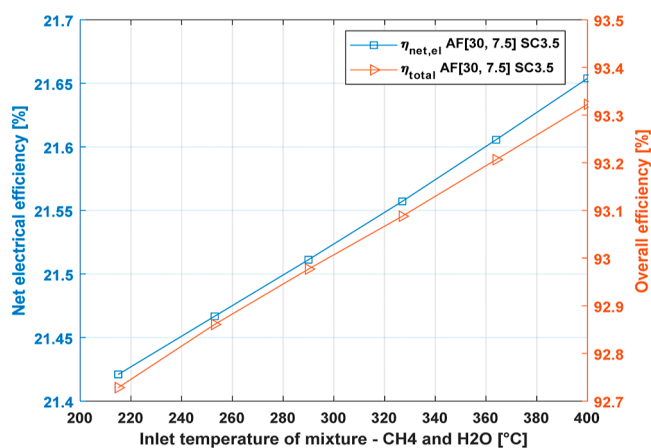

Figure 15. Effect of the inlet temperature of distilled water steam on system efficiencies.

and WGS reactor on the system efficiencies are analyzed respectively. The decrease of the afterburner's outlet temperature (T_{burner}) from 850 to 800 °C results in the decrease of the SMR conversion from 97.3 to 95.6%. According to the relation between the auxiliary methane and excess of air, the A/F factor was kept constant, while the air and auxiliary methane flows were adjusted to vary the T_{burner}.

As can be seen in Figure 16a, the overall and net electrical efficiencies decrease from 92.9 to 73.7% and from 21.5 to 13.6%, respectively, when the afterburner temperature is decreased. The molar fraction of hydrogen in the syngas is set to be constant, and the process methane flow rate is adjusted to ensure the hydrogen yield and satisfy the demand for electricity production. With decreasing T_{burner}, the conversion of SMR is slightly reduced, which leads to a higher requirement in process methane, which in turn causes the reduction of system efficiencies.

Figure 16b presents the influence of the outlet temperature of the WGS reactor. This outlet temperature (T_{WGS}) is varied from 300 to 260 °C. By decreasing T_{WGS}, which favors the transformation of carbon monoxide, no significant impact on the electrical efficiency is observed, whereas a decrease in the CO content from 1.1 to 0.6% in the syngas is observed. It is important to notice that the fuel quality should always be controlled and regulated to be below the maximum limit of 3% for carbon monoxide concentration recommended by the fuel cell manufacturer. The presence of contaminants in the reformate gas will also have impacts on performance and, in some cases, on the lifetime of the fuel cell.

By analyzing the system sensitivity for full-load operation and under the defined optimal operating conditions (S/C = 3.5, A/F = 30, T_{burner} = 850 °C, $T_{mixture}$ = 253 °C, and T_{WGS} = 300 °C), a net electrical efficiency of 21.5% is achieved. An optimal net electrical efficiency of 47.3% was also obtained at 7% partial load, which is significantly higher than the efficiency that could be obtained using electrical generation of 1 kW.

All along this sensitivity analysis, all observed trends were regular: no limitation related to local pinch appeared, indicating that the compact heat-exchanger reactor is a flexible unit that does not constrain the optimization of the micro-CHP process.

3.4. Exchange Network. A pinch analysis is performed for the current process plant, using a value of ΔT_{min} equal to 10 °C. The process integration is a suitable methodology for minimizing process energy consumption by calculating
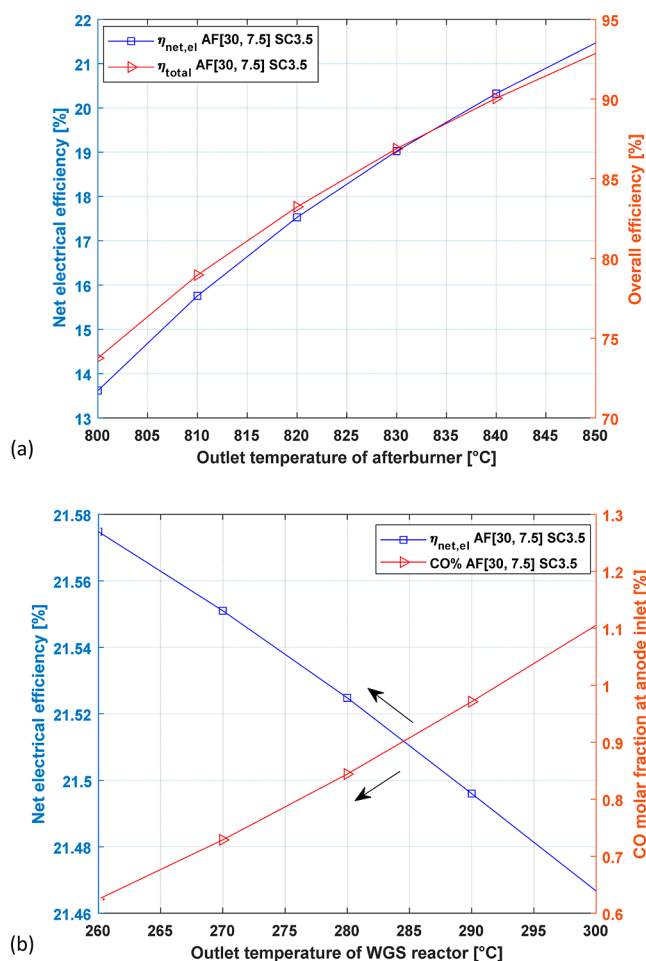
Figure 16. (a) Effect of the afterburner outlet temperature on system efficiencies and (b) effect of the WGSR outlet temperature on the CO molar fraction at anodic inlet and net electric efficiency.

minimum thermodynamically feasible energy consumption targets and approaching them by optimizing the energy recovery system, utility input, and process operating conditions. The implementation of such a pinch analysis on an industrial process leads to substantial economies.

The objective of this analysis is to respect the existing process configuration and to add exchangers in order to have an adapted exchange network. As detailed below, this specific problem corresponds to the existing process configuration related to the "threshold problems,"[42] requiring the addition of three heat-exchangers (as shown in Figure 17), called "evapo," "echa-in," and "e-fc 1"). The heat recovered by the syngas leaving the SMR reactor [H1(a,b)] is used to preheat the input process streams C1 and C2 (distilled water and process methane). The hot exhaust gas leaving the SMR reactor (H2) is used to preheat the inlet air at the cathode of the stack (C3).

Table 10 details the heat exchanger network information. Streams C1 and C2 are preheated from 137 to 609 °C and from 43 to 330 °C, respectively, by stream H1(a,b), transferring a total of 258 W. The air entering the cathode (stream C3) is preheated by the combustion exhaust gas (stream H2) coming from the SMR reactor. A heat flow of 197 W is required to obtain stream at 160 °C. Therefore, three heat exchangers are required in order to satisfy the internal heating demands in accordance with the current process configuration.

Figure 18 presents the composite curves: the cold composite curve, which needs to be heated, is totally covered by the hot composite curve, which means that no external hot utility is required. All necessary heat can be provided by the hot process streams (mainly the hot exhaust from the combustion). On the other hand, no cold streams are available between 0 and approximately 820 W of the hot composite curve, which indicates that supplementary cooling is necessary. This heat is supposed to be recovered by domestic heating demands or sanitary hot water production. The profile of the obtained composite curve corresponds to the first type of the "threshold problems,"[42] in which the closest temperature approach between the hot and cold composites is at the "non-utility" end and the curves diverge away from this point, as shown in Figure 18.

The solution proposed by the pinch analysis is to match the hottest hot stream with the hottest cold stream, and maintain the chosen value of the ΔT_{min} criterion. Nevertheless, in order to minimize the number of exchange units and to maximize the potential heat exchange in the process, the design strategy consists in matching the less hot stream [H1(a)] with the hottest cold stream (C2) first, then [H1(b)] to transfer with the coldest cold stream (C1). To do so, the stream H1 can be fully valorized by bringing stream C2 and C1 up to 609 and 330 °C, respectively. Likewise, stream H2 can be matched against stream C3, to heat it up to 160 °C. Thereafter, the remaining heat of stream H2 will be recovered by a recuperator for further exchange use according to our needs.

Therefore, since the temperatures of the entering process streams have been increased, the temperature of the reactant mixture reaches approximately 525 °C, and the thermal and net electrical efficiencies of the process can be further improved at 71.9 and 21.9%, respectively. This gain in system efficiencies does not appear substantial and should be quantified properly in a techno-economic analysis by considering the capitalistic expenditures associated with the three additional heat exchangers required.

4. CONCLUSIONS

In the present study, simulation models of a compact millistructured heat-exchanger reactor and a HT-PEM fuel cell have been validated on the basis of experimental measurements and integrated into the complete simulation of the 1 kW HT-PEM fuel-cell-based micro-CHP plant by using the simulation software ProSimPlus. The results obtained, on one hand, from the model and, on the other hand, from the experimental pilot plant of the micro-cogenerator have been compared and discussed. A parametric analysis has been performed, including the influence of fuel partialization, the combined impact of the A/F factor S/C ratio, the inlet temperature of distilled water, and the outlet temperature of the afterburner and WGS reactor.

In the fuel partialization strategy, the provided fuel was gradually reduced down to 7.3% of its initial value, demonstrating that the gross electrical power can be diminished from 1018 W under full load conditions down to 113.2 W and that the thermal production can be reduced from 1445 to 86.3 W. In the same time, the electrical efficiency is improved from 21.5 to 47.4% and the thermal efficiency is increased from 71.4 to 75.4%. This flexibility of the complete process was not compromised by the compact heat-exchanger reactor and the integration heat-exchangers. In this analysis of the operating conditions, the best performances are obtained with different values of A/F in combination with higher values of the S/C ratio
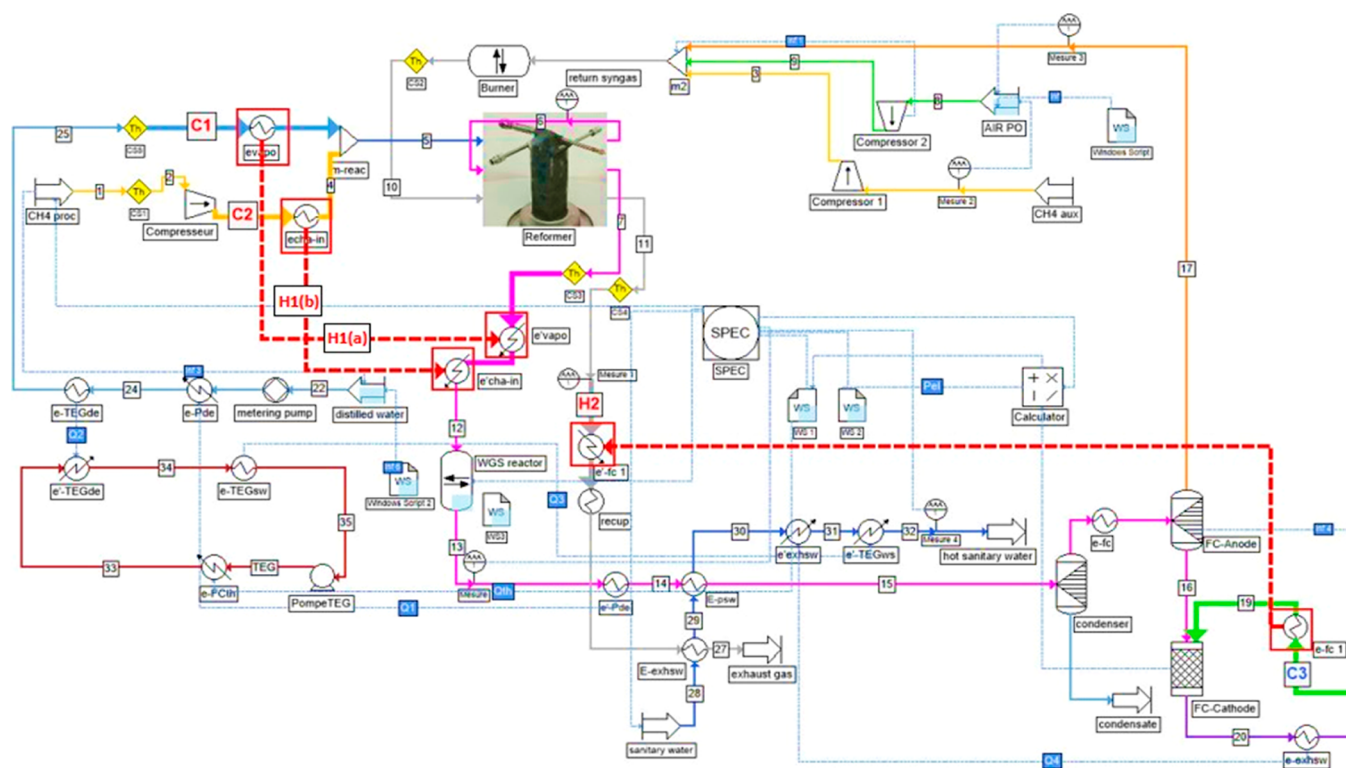
Figure 17. Exchange network of micro-CHP process by applying the pinch analysis.

Table 10. Hot and Cold Streams Heat Exchange Information

stream	description	$\dot{m} \cdot C_p$ (W K^{-1})	initial temperature (°C)	final temperature (°C)	hot/cold utility (W)
H1	syngas coming out of the SMR	0.76	619	280	−258
H2	exhaust gas coming out of the SMR	2.90	648	300	−1012
C1	process CH$_4$ coming out of the compressor	0.16	43	330	44
C2	distilled water (after exchange with TEG loop)	0.45	137	609	213
C3	inlet air at cathode	1.74	48	160	197

Figure 18. Composite curves of the hot and cold process streams.

(≥ 3.5). Among the optimal operating conditions, the case of the A/F ratio equal to [30, 7.5] and the S/C ratio equal to 3.5 was chosen for the inlet/outlet component's temperature analysis. A final pinch analysis enabled us to propose a process exchange network that still increased the electrical and thermal efficiency up to 21.9 and 71.9%, respectively, by adding three new heat exchangers. Ersoz et al.[43] worked on newly designed "micro scale compact fuel processing system" for hydrogen-rich gas production to be used for a 1 kWe high-temperature fuel cell (HTPEM) and achieved electrical efficiency in the range of 21−29% and an overall efficiency of about 80−90%. Both studies demonstrate that to improve the electrical efficiency of the system, it is necessary to optimize the system with the parameters mentioned in this study.

To properly optimize the CHP plant and propose a process structure and corresponding operating conditions, the analysis performed in this work should be completed by exploiting the complete model in the framework of a multi-objective optimization. As demonstrated above, optimal solutions should

consider not only the electrical and thermal efficiency as technical objectives but also the economic criteria related to the need for additional integration heat exchangers, environmental criteria related to the total methane consumption, and versatility criteria to accommodate specific thermal and electrical load requirements for full load and fuel partialization operations. Exergy analysis could also be beneficial to identify units whose optimization should be prioritized. Management strategies could then be proposed to ensure continuous optimality while providing flexibility to the users. In addition, from a technical point of view, a detailed analysis of simulation errors should be performed to quantify their impact on the key performance indicators: a Monte-Carlo type approach could be applied to

consider uncertainties related to kinetic parameters of the reactive units, non-linearities related to process units and recycle structures, convergence steps and numerical schemes of the used software, as well as unit models and underlying assumptions.

■ APPENDIX

A. Theoretical HT-PEMFC Model Demonstration

The theoretical HT-PEMFC model is simplified from a three-dimensional HT-PEMFC model.[32,44−46] The main assumptions of this model consider that

- All the reactors and the fuel cell of the HT-PEMFC system operate in steady state.
- The CO poisoning effect on the HT-PEMFC stack performance is neglected. It was reported experimentally and numerically that the CO poisoning effect was diminished at the operating temperature of 160 °C for 2% CO in the anode feed stream. Therefore, this assumption is reasonable at a higher operating temperature (>160 °C) and/or lower CO content (<1%).

The HT-PEMFC system model was implemented in a commercial flow diagram simulator, ASPEN HYSYS, and then applied to the 5 kWe HT-PEMFC system. The model was first validated against in-house test data, and successfully reproduced the measured exhaust gas compositions and reactor temperatures from the experiments.

To implement this model, the cell voltage, V_{cell}, can be determined after estimating the activation loss η_{act}, ohmic loss η_{ohm}, and concentration loss η_{con}; thus, the thermodynamic equilibrium potential, E_{Nernst}, is described as

$$V_{cell} = E_{Nernst} - \eta_{act} - \eta_{ohm} - \eta_{con} \qquad (14)$$

In order to determine the expression of E_{Nernst}, one needs to determine first the expression of the thermodynamic electromotive force (EMF), E_0, of one cell from the Gibbs energy of combustion under the standard conditions ($P_0 = 1$ bar and $T_0 = 25$ °C). This is given by eq 15, where n denotes the number of electrons released by the oxidation of a fuel molecule (two electrons for a molecule of hydrogen).[47]

$$E^0 = \frac{-\Delta_r G^\theta}{n\mathcal{F}} \qquad (15)$$

Under standard conditions, the Gibbs energy of combustion of hydrogen is $\Delta_r G^\theta = -237.13$ kJ mol^{-1} H$_2$, which yields $E^0 = 1.23$ V.

The standard voltage depends only on the type of fuel used. The reversible voltage of one cell (E_{Nernst}), determined by using the Nernst eq 16,[48] considers the temperature of the cell (assumed to be uniform) and the chemical activity of the reactants and products of the electrochemical reaction. This activity is denoted by α; α^r is the activity of a reactant and α^p is the activity of a product. γ_r and γ_p represent the molar stoichiometric coefficients of the reactants and products. The expression $E^0(T)$ denotes that the cell voltage is determined from the previous expression at the operating temperature of the fuel cell.

$$E_{Nernst} = \frac{-\Delta_r G}{n\mathcal{F}} = E^0(T) + \frac{RT}{n\mathcal{F}} \times \ln\left(\frac{\prod \alpha_r^{\gamma_r}}{\prod \alpha_p^{\gamma_p}}\right) \qquad (16)$$

As the fuel cell operates at high temperature, the steam behavior can be assumed to be ideal.[48] However, for ideal gas, the chemical activity of reactants and products can be represented by the partial pressure of each component at high temperature, where the partial pressures of each component are represented by the operating pressure of the fuel cell (P). In the case of a fuel cell running on hydrogen, eq 16 can, therefore, be replaced by eq 17

$$E_{Nernst} = \frac{-\Delta_r G}{n\mathcal{F}}$$

$$= E^0(T) + \frac{RT}{n\mathcal{F}} \times \ln\left(\frac{\alpha \times \beta^{1/2}}{\gamma}\right) + \frac{RT}{2n\mathcal{F}} \times \ln(P) \qquad (17)$$

This relation shows that the voltage increases with the pressure and with the concentration of hydrogen or oxygen. As observed from this expression, for a HT-PEM fuel cell, the theoretical value of E_{Nernst} is about 1.12 V at an operating temperature assumed to be 160 °C.

As shown in eq 14, the activation overvoltage, η_{act}, represents the overall activation loss on the anode side due to the hydrogen oxidation reaction (HOR) and the activation loss on the cathode side due to the oxygen reduction reaction (ORR). The anode and cathode activation losses can be estimated from the Butler−Volmer (B−V) equations for HOR and ORR, as described in eqs 18−20

$$\eta_{act} = \eta_{act,a} + |\eta_{act,c}| \qquad (18)$$

$$\eta_{act,a} = \frac{i}{i_{0,a}^{ref}} \times \frac{RT}{(\alpha_a + \alpha_c) \times \mathcal{F}} \times \left(\frac{C_{H_2}^{ref}}{C_{H_2}}\right)^{1/2} \qquad (19)$$

$$|\eta_{act,c}| = \frac{RT}{\theta_c \times \mathcal{F}} \times \ln\left[\left(\frac{C_{O_2}^{ref}}{C_{O_2}}\right)^{3/4} \times \frac{i}{i_{0,c}^{ref}}\right] \qquad (20)$$

In eqs 19 and 20, C_i is the molar concentration at the surface of the catalyst in the anode and cathode of species i, θ is the transfer coefficient, and $i_{0,a}^{ref}$ and $i_{0,c}^{ref}$ are the exchange current densities for HOR and ORR, respectively, expressed by eqs 21 and 22

$$i_{0,a}^{ref}(T) = i_{0,a}^{ref}(353.15 \text{ K}) \times \exp\left[-1400 \times \left(\frac{1}{T} - \frac{1}{353.15}\right)\right] \qquad (21)$$

$$i_{0,c}^{ref}(T) = i_{0,c}^{ref}(353.15 \text{ K}) \times \exp\left[-7900 \times \left(\frac{1}{T} - \frac{1}{353.15}\right)\right] \qquad (22)$$

The ohmic losses are mainly caused by the resistances to proton transfer through the membrane and catalyst layers. Electron transfer resistances across the catalyst layers, as well as the gas diffusion layers (GDLs) and flow field plates, are generally very low compared to ionic resistances. Contact resistances, which occur primarily at the interface between GDLs and flow field plates, are a function of the surface condition, material roughness, and contact pressure between the materials.[32] Assuming that the HOR and ORR take place in the middle of the catalyst layers, and neglecting the contact resistances, the total ohmic loss can be expressed as

$$\eta_{ohm} = i \times (R_{H^+} + R_{elec}) \qquad (23)$$

In eqs 24 and 25, R_{H^+} and R_{elec} represent the specific resistances due to proton and electron transport, respectively.

Table 11. Theoretical Expressions and Significations of the Coefficients of the Selected Model

coefficient	theoretical expression	description
a_1	E_{Nernst}	cell reversible tension
a_2	$\left(\dfrac{1}{i_{0,a}^{\text{ref}}} \times \dfrac{RT}{(\alpha_a + \alpha_c) \times \mathcal{F}} \times \left(\dfrac{C_{H_2}^{\text{ref}}}{C_{H_2}} \right)^{1/2} \right) + (R_{H^+} + R_{\text{elec}})$	coefficient resulting from the combination of the anodic activation loss and the ohmic loss terms, respectively
a_3	$\dfrac{RT}{\alpha_c \times \mathcal{F}}$	coefficient related to the cathodic transfer coefficient
a_4	$C_{O_2}^H$	equilibrium molar concentration of oxygen obtained by Henry's law
a_5	$\dfrac{\delta_m}{4\mathcal{F} \times D_{O_2}^{\text{PA}} \times \frac{r_{\text{agg}}}{r_{\text{agg}} + \delta_m}}$	coefficient of the oxygen diffusion term at the catalyst surface

The latter can be determined by the given properties and dimensions of the membrane, GDLs, and catalyst layer (CL)

$$R_{H^+} = \frac{\delta_{\text{mem}}}{\kappa} + \frac{0.5 \times \delta_{\text{acl}}}{v_{\text{acl}}^{1.5} \times \kappa} + \frac{0.5 \times \delta_{\text{ccl}}}{v_{\text{ccl}}^{1.5} \times \kappa} \tag{24}$$

$$R_{\text{elec}} = \frac{0.5 \times \delta_{\text{acl}} + 0.5 \times \delta_{\text{ccl}} + \delta_{\text{aGDL}} + \delta_{\text{cGDL}}}{\kappa_e} \tag{25}$$

where v_{acl} and v_{ccl} are the volume fractions of ionomer in the CLs of anode and cathode, δ_{acl} and δ_{ccl} are the thicknesses of CLs of electrodes, and δ_{aGDL} and δ_{cGDL} are the thicknesses of the GDLs of the anode and cathode, respectively.

The expression for the concentration overvoltage, η_{con} is given by eq 26

$$\eta_{\text{con}} = \frac{RT}{4\mathcal{F}} \times \ln \left(\frac{i_{\lim}}{i_{\lim} - i} \right) \tag{26}$$

In eq 26, $i_{\lim}$ is the limiting current density, which is a function of the oxygen concentration at the interface of the GDL and the gas channel, $C_{O_2}^{\text{int}}$, as well as of the porosity of the GDL (v_{GDL}), and of the tortuosity and the thickness of the cathodic GDL (δ_{GDL}). The expression is given by eq 27

$$i_{\lim} = n \times \mathcal{F} \times v_{\text{GDL}}^{1.5} D_{O_2} \times \frac{C_{O_2}^{\text{int}}}{\delta_{\text{GDL}}} \tag{27}$$

By substitution of the overvoltage expressions in the cell voltage expression, eq 28 is finally obtained, enabling us to establish a theoretical model structure to identify the parameters

$$\begin{aligned} V_{\text{cell}} = E_{\text{Nernst}} &- \frac{i}{i_{0,a}^{\text{ref}}} \times \frac{RT}{(\alpha_a + \alpha_c) \times \mathcal{F}} \times \left(\frac{C_{H_2}^{\text{ref}}}{C_{H_2}} \right)^{1/2} \\ &- \frac{RT}{\alpha_c \times \mathcal{F}} \times \ln \left[\left(\frac{C_{O_2}^{\text{ref}}}{C_{O_2}} \right)^{3/4} \times \frac{i}{i_{0,c}^{\text{ref}}} \right] \\ &- i \times (R_{H^+} + R_{\text{elec}}) - \frac{RT}{4\mathcal{F}} \times \ln \left(\frac{i_{\lim}}{i_{\lim} - i} \right) \end{aligned} \tag{28}$$

From expression (eq 28), it is possible to write the first three terms as a function of current density, without considering the concentration loss term. In fact, this term does not yield to a significant effect on the evolution of cell voltage as a function of current density in the current operating range. Furthermore, the

molar oxygen concentration can be expressed as a function of the current density described by Fick's law given by eq 29.[32,49]

$$N_{O_2} = \frac{i}{4\mathcal{F}} = D_{O_2}^{\text{PA}} \times \frac{r_{\text{agg}}}{r_{\text{agg}} + \delta_m} \times \frac{C_{O_2}^H - C_{O_2}}{\delta_m} \tag{29}$$

Thus, a new expression of the correlation of voltage V_{cell} as a function of the current density i with five coefficients (a_1, a_2, a_3, a_4, and a_5) is given by eq 30

$$V_{\text{cell}} = a_1 - a_2 \times i + a_3 \times \ln \left(\frac{\left(\frac{C_{O_2}^{\text{ref}}}{a_4 - a_5 \times i} \right)^{-3/4} \times i_{0,c}^{\text{ref}}}{i} \right) \tag{30}$$

The model is based on eq 30 and inspired by the form of the theoretical expression, which represents each corresponding phenomenon with precision and includes linear and logarithmic effects with regard to the current density. The expressions of the coefficients can, therefore, be identified by comparison with the theoretical expression, and their significations are presented in Table 11.

To adjust the parameters a_1 to a_5, the sum of squares of the differences between the experimental measurements and the modeled cell voltages (eq 31) is minimized using a genetic algorithm. In eq 31, n_{exp} is the total number of experimental points taken from the polarization curve, and $i_{\text{exp},k}$ and $V_{\text{exp},k}$ respectively, denote the measured current density and voltage of the experimental data k

$$J = \sum_{k=1}^{k=n_{\text{exp}}} [f(i_{\text{exp},k}) - V_{\text{exp},k}]^2 \tag{31}$$

During the optimization of the coefficients, in some cases, the values used in the optimizer for the coefficients a_4 and a_5 might induce a complex value of the potential (V_{cell}). An identifiability analysis was performed to assess the sensitivity of the criterion J with respect to the coefficients a_1, a_2, a_3, a_4, and a_5: the sensitivity of the criterion with respect to a_4 and a_5 is very low, preventing their reliable identification. Instead of leaving the coefficients a_4 and a_5 completely independent, lower and upper bounds, issued from the theory, have been imposed, and these restricted ranges of variations enabled us to minimize the criterion while keeping the optimization unconstrained for the coefficients a_1, a_2, and a_3. The values obtained for the coefficients a_4 and a_5 are 0.57 and 4.45×10^{-6}, respectively. However, since they do not exhibit sufficient sensitivity for proper identification, their confidence

intervals have not been calculated. Table 12 shows the values of the identified coefficients including their confidence intervals

Table 12. Values of the Coefficients Obtained by Optimization and Estimations Based on Theory[a]

	optimal identified value	value ranges expected from theoretical estimation	
		lower bound	upper bound
a_1	0.43 ± 0.00506	1.10	1.15
a_2	0.22 ± 0.0113	0.089	0.29
a_3	0.059 ± 0.115	0.042	0.062
a_4	0.57	0.26	3.48
a_5	4.45×10^{-6}	3.60×10^{-6}	1.58×10^{-4}

[a]The values of the operating conditions and parameters used for the theoretical estimation of the coefficients are summarized in Table 13.

Table 13. Geometrical/Operating Conditions and Input Parameters for HT-PEMFC Modeling

parameter	unit	value	refs
operating temperature,	°C	160	—
stoichiometry A/C, λ_a, λ_c	—	1.35/2.5	—
number of cells	—	50	—
active surface, A_{MEA}	cm^2	163.5	—
pressure at the A/C inlet, P	atm	1	—
transfer coefficient A/C, α_a, α_c	—	0.5/0.65, 0.89	32, 49
proton conductivity of the membrane, κ	S m^{-1}	13, 36.22	32, 49
electron conductivity of GDL, κ_e	S m^{-1}	1250, 687.5	44, 50
mass fraction of H$_3$PO$_4$, m_{H3PO4}	wt %	55 ± 4.85	50, 51
doping level of H$_3$PO$_4$, X	—	6.2, 32	44, 49
thickness of the membrane, δ_{mem}	m	152×10^{-6}	49
thin electrolyte film thickness, δ_m	m	5.47×10^{-8}	44
thickness of CLs A/C, δ_{acl}, δ_{ccl}	m	3.0×10^{-6}/ 4.0×10^{-6}	49
thickness of GDLs A/C, δ_{aGDL}, δ_{cGDL}	m	5.5×10^{-4}	50
ref. molar concentration, $C_{H_2}^{ref}$, $C_{O_2}^{ref}$	mol m^{-3}	40.88	32
molar mass of PBI, MPBI	kg mol^{-1}	0.308	49
molar mass of H$_3$PO$_4$, M$_{H3PO4}$	kg mol^{-1}	0.098	49
ref. exchange current density A/C, $i_{0,a}^{ref}$, $i_{0,c}^{ref}$	A m^{-2}	10^9/10^4	32
agglomerate radius, r_{agg}	m	10^{-6}	47
volume fractions of ionomer in CLs, v_{acl}, v_{ccl}	vol %	0.3, 0.4	32, 44

(minimum criterion value in the order of 10^{-4}), the ranges of the coefficients obtained by the theoretical estimation. The comparison of this model with the experimental data is presented in Figure 8.

■ AUTHOR INFORMATION

Corresponding Author

Di Wu − *Laboratoire Réactions et Génie des Procédés, UMR 7274, Université de Lorraine, CNRS, Nancy F-54000, France; AUER, Feuquières-en-Vimeu 80210, France;* ● orcid.org/0000-0001-7671-9263; Email: di.wu@univ-lorraine.fr

Authors

Jean-Marc Commenge − *Laboratoire Réactions et Génie des Procédés, UMR 7274, Université de Lorraine, CNRS, Nancy F-54000, France;* ● orcid.org/0000-0003-2792-9357

Emilien Fort − *AUER, Feuquières-en-Vimeu 80210, France*

Claire Hardy − *AUER, Feuquières-en-Vimeu 80210, France*

Jérôme Pecquery − *AUER, Feuquières-en-Vimeu 80210, France*

Laurent Falk − *Laboratoire Réactions et Génie des Procédés, UMR 7274, Université de Lorraine, CNRS, Nancy F-54000, France*

Complete contact information is available at:
https://pubs.acs.org/10.1021/acsomega.3c01143

■ NOMENCLATURE

A/F	air-to-fuel factor
BOP	balance of plant
CHP	combined heat and power
CLs	catalyst layers
C/H	cold/hot
EMF	thermal electromotive force
GDLs	gas diffusion layers
HT-PEM	high temperature proton exchange membrane
LT-PEM	low temperature proton exchange membrane
MEA	membrane electrode assembly
PA	phosphoric acid
PBI	polybenzimidazole
RF	reforming factor
S/C	steam-to-carbon ratio
SMR	steam methane reforming
SOFC	solid oxide fuel cell
sw	sanitary water
TEG	triethylene glycol
WGS	water gas shift

■ SYMBOLS

$A_{SMR\ surface}$	pre-exponential factor of the reaction SMR, mol m$_{ams}^{-2}$ s^{-1} bar^{-2}
A_m	surface of active metal per mass of active metal, m$_{ams}^2$ g$_{metal}^{-1}$
C	concentration, mol m^{-3}
C_p	heat capacity, kJ kg^{-1} K^{-1}
D	diffusion coefficient, m^2 s^{-1}
E_a	activation energy, kJ mol^{-1}
E_{Nernst}	thermodynamic equilibrium potential, V
$\mathcal{F}$	Faraday constant, C mol^{-1}
$\Delta_r G^\theta$	standard Gibbs energy kJ kmol^{-1}
i	current density, A cm^{-2}
K_μ	microstructure constant, m$_{active\ surface}^2$ m$_{catalyst}^{-2}$
K	equilibrium constant, —
LHV	low heating value, kJ mol^{-1}
M_c	mass of catalyst deposited per projected area m^2 g^{-1}
N_{O_2}	molar concentration of oxygen, mol m^{-2} s^{-1}

n	number of cells, —
$\dot{n}$	molar flow rate, mol s^{-1}
PR	active metal content of the catalyst, %
P_i	partial pressure of species i, Pa
P	power, W
Q	thermal heat, W
R	universal gas constant, kJ kmol^{-1} K^{-1}
R_{H^+}	specific resistances due to proton transport, Ω
R_{elec}	specific resistances due to electron transport, Ω
R_{SMR}	reaction rate, mol L$_{reactor}^{-1}$ s^{-1}
T	temperature, K
V	voltage, V
X	membrane doping level, —

■ SUBSCRIPTS

A/a	anode
agg	agglomerate radius
ams	active metal surface
C/c	cathode
el	electrical
lim	limiting current density
mem	membrane
MEA	membrane electrode assembly
0	standard condition
p	product
r	reactant
ref	reference value
th	thermal

■ GREEK SYMBOLS

α	activity
δ	thickness, m
ε	efficiency
$\eta_{act,a}$	anodic voltage loss
$\eta_{act,c}$	cathodic voltage loss
η_{con}	concentration loss
η_{el}	electrical efficiency
η_{ohm}	ohmic loss
η_{th}	thermal efficiency
η_{total}	global efficiency
θ	transfer coefficient
κ	proton conductivity, S m^{-1}
λ	stoichiometric ratio
ν	porosity
ρ	density, kg m^{-3}
υ	volume fractions of ionomer

■ REFERENCES

(1) De Groote, M.; Rapf, O. *Discussion Paper: The Active Role of Buildings in a Transforming Energy Market*; Buildings Performance Institute Europe, 2015.

(2) Atanasiu, B.; Maio, J. *Europe's Buildings under the Microscope. A Country-by-Country Review of the Energy Performance of Buildings*; Buildings Performance Institute Europe, 2011.

(3) Merkel, E.; McKenna, R.; Fehrenbach, D.; Fichtner, W. A model-based assessment of climate and energy targets for the German residential heat system. *J. Cleaner Prod.* **2017**, *142*, 3151–3173.

(4) Valentin, L.; Dabbagh, M.; Krarti, M. Benefits of switchable insulation systems for residential buildings in France. *Energy Build.* **2022**, *259*, 111868.

(5) Construction et performance environnementale du bâtiment. https://www.ecologie.gouv.fr/construction-et-performance-environnementale-du-batiment (accessed Aug 22, 2022).

(6) Réglementation environnementale RE2020. https://www.ecologie.gouv.fr/reglementation-environnementale-re2020 (accessed Aug 22, 2022).

(7) Ahmed, A.; Ge, T.; Peng, J.; Yan, W. C.; Tee, B. T.; You, S. Assessment of the renewable energy generation towards net-zero energy buildings: A review. *Energy Build.* **2022**, *256*, 111755.

(8) Boudellal, M. *Cogénération et micro-cogénération*, 2nd ed.; Dunod, 2013.

(9) Arsalis, A. A comprehensive review of fuel cell-based micro-combined-heat-and-power systems. *Renewable Sustainable Energy Rev.* **2019**, *105*, 391–414.

(10) Environmental Protection Agency. Combined Heat and Power (CHP) Partnership. https://www.epa.gov/chp/what-chp (accessed Nov 25, 2022).

(11) Renau, J.; García, V.; Domenech, L.; Verdejo, P.; Real, A.; Giménez, A.; Sánchez, F.; Lozano, A.; Barreras, F. Novel Use of Green Hydrogen Fuel Cell-Based Combined Heat and Power Systems to Reduce Primary Energy Intake and Greenhouse Emissions in the Building Sector. *Sustainability* **2021**, *13*, 1776.

(12) Pehnt, M. Environmental impacts of distributed energy systems—The case of micro cogeneration. *Environ. Sci. Policy* **2008**, *11*, 25–37.

(13) Lepiksaar, K.; Mašatin, V.; Latõšov, E.; Siirde, A.; Volkova, A. Improving CHP flexibility by integrating thermal energy storage and power-to-heat technologies into the energy system. *Smart Energy* **2021**, *2*, 100022.

(14) Simader, G. R.; Krawinkler, R.; Trnka, G. Micro CHP systems: state-of-the-art. 2006, https://energiatalgud.ee/sites/default/files/images_sala/f/fd/Micro_CHP_systems._State_of_the_Art.pdf (accessed Aug 22, 2022). .

(15) European Commission. EU Buildings Factsheets. https://ec.europa.eu/energy/eu-buildings-factsheets_en (accessed Nov 25, 2022).

(16) Andlauer, B. Optimisation systémique de micro-cogénérateurs intégrés au bâtiment. Ph.D. Dissertation, Paris Institute of Technology, Paris, 2014. https://pastel.archives-ouvertes.fr/pastel-01073341 (accessed 2022 08 22).

(17) Elmer, T.; Worall, M.; Wu, S.; Riffat, S. B. Fuel cell technology for domestic built environment applications: State of-the-art review. *Renewable Sustainable Energy Rev.* **2015**, *42*, 913–931.

(18) Özgür, T.; Yakaryılmaz, A. C. A review: Exergy analysis of PEM and PEM fuel cell based CHP systems. *Int. J. Hydrogen Energy* **2018**, *43*, 17993–18000.

(19) Braun, R. J.; Klein, S. A.; Reindl, D. T. Evaluation of system configurations for solid oxide fuel cell-based micro-combined heat and power generators in residential applications. *J. Power Sources* **2006**, *158*, 1290–1305.

(20) Onovwiona, H. I.; Ugursal, V. I. Residential cogeneration systems: review of the current technology. *Renewable Sustainable Energy Rev.* **2006**, *10*, 389–431.

(21) Ellamla, H. R.; Staffell, I.; Bujlo, P.; Pollet, B. G.; Pasupathi, S. Current status of fuel cell based combined heat and power systems for residential sector. *J. Power Sources* **2015**, *293*, 312–328.

(22) Jannelli, E.; Minutillo, M.; Perna, A. Analyzing microcogeneration systems based on LT-PEMFC and HT-PEMFC by energy balances. *Appl. Energy* **2013**, *108*, 82–91.

(23) Korsgaard, A. R.; Nielsen, M. P.; Kær, S.K. Part one: A novel model of HTPEM-based micro-combined heat and power fuel cell system. *Int. J. Hydrogen Energy* **2008**, *33*, 1909–1920.

(24) Korsgaard, A. R.; Nielsen, M. P.; Kær, S.K. Part two: Control of a novel HTPEM-based micro combined heat and power fuel cell system. *Int. J. Hydrogen Energy* **2008b**, *33*, 1921–1931.

(25) Zhang, J.; Xie, Z.; Zhang, J.; Tang, Y.; Song, C.; Navessin, T.; Shi, Z.; Song, D.; Wang, H.; Wilkinson, D. P.; Liu, Z. S.; Holdcroft, S. High temperature PEM fuel cells. *J. Power Sources* **2006**, *160*, 872–891.

(26) Arsalis, A.; Kær, S. K.; Nielsen, M. P. Modeling and optimization of a heat-pump-assisted high temperature proton exchange membrane fuel cell micro-combined-heat-and-power system for residential applications. *Appl. Energy* **2015**, *147*, 569–581.

(27) Baharudin, L.; Indera L, A. A.; Watson, M. J.; Yip, A. C. K. Process intensification in multifunctional reactors: A review of multi-functionality by catalytic structures, internals, operating modes, and unit integrations. *Chem. Eng. Process.* **2021**, *168*, 108561.

(28) Mbodji, M.; Commenge, J. M.; Falk, L.; di Marco, D.; Rossignol, F.; Prost, L.; Valentin, S.; Joly, R.; Del-Gallo, P. Steam methane reforming reaction process intensification by using a millistructured reactor: Experimental setup and model validation for global kinetic reaction rate estimation. *Chem. Eng. J.* **2012**, *207−208*, 871−884.

(29) Commenge, J. M.; Falk, L.; Corriou, J. P.; Matlosz, M. Analysis of Microstructured Reactor Characteristics for Process Miniaturization and Intensification. *Chem. Eng. Technol.* **2005**, *28*, 446−458.

(30) Najafi, B.; Haghighat Mamaghani, A.; Baricci, A.; Rinaldi, F.; Casalegno, A. Mathematical modelling and parametric study on a 30 kWel high temperature PEM fuel cell based residential micro cogeneration plant. *Int. J. Hydrogen Energy* **2015**, *40*, 1569−1583.

(31) Najafi, B.; Haghighat Mamaghani, A.; Rinaldi, F.; Casalegno, A. Fuel partialization and power/heat shifting strategies applied to a 30 kWel high temperature PEM fuel cell based residential micro cogeneration plant. *Int. J. Hydrogen Energy* **2015b**, *40*, 14224−14234.

(32) Gwak, G.; Kim, M.; Kim, D.; Faizan, M.; Oh, K.; Lee, J.; Choi, J.; Lee, N.; Lim, K.; Ju, H. Performance and efficiency analysis of an HT-PEMFC system with an absorption chiller for tri-generation applications. *Energies (Basel)* **2019**, *12*, 905.

(33) Oh, K.; Chippar, P.; Ju, H. Numerical study of thermal stresses in high-temperature proton exchange membrane fuel cell (HT-PEMFC). *Int. J. Hydrogen Energy* **2014a**, *39*, 2785−2794.

(34) Won, S.; Oh, K.; Ju, H. Numerical degradation studies of high-temperature proton exchange membrane fuel cells with phosphoric acid-doped PBI membranes. *Int. J. Hydrogen Energy* **2016**, *41*, 8296−8306.

(35) Oh, K.; Jeong, G.; Cho, E.; Kim, W.; Ju, H. A CO poisoning model for high-temperature proton exchange membrane fuel cells comprising phosphoric acid-doped polybenzimidazole membranes. *Int. J. Hydrogen Energy* **2014**, *39*, 21915−21926.

(36) ProSimPlus software—Steady-state simulation and optimization of processes. 2022, https://www.prosim.net/en/product/prosimplus-steady-state-simulation-and-optimization-of-processes/ (accessed Aug 22, 2022).

(37) Bruschi, Y. M.; López, E.; Schbib, N. S.; Pedernera, M. N.; Borio, D. O. Theoretical Study of the Ethanol Steam Reforming in a Parallel Channel Reactor. *Int. J. Hydrogen Energy* **2012**, *37*, 14887−14894.

(38) Mbodji, M. Conception et dimensionnement de réacteurs-échangeurs microstructurés pour la production de gaz de synthèse par vaporeformage du méthane. Ph.D. Dissertation, LRGP, University of Lorraine, Nancy, 2013. https://hal.archives-ouvertes.fr/tel-01750537 (accessed 2022 08 22).

(39) Barbé, J. P. Modélisation des échangeurs-réacteurs compacts. PhD thesis, Université de Lorraine, 2018.

(40) Siemens. Ultramat 23 for IR-absorb. Industry Support, https://support.industry.siemens.com/cs/document/7600621/ultramat-23-for-ir-absorbing-gases-and-oxygen?dti=0&lc=en-AE (accessed Aug 22, 2022).

(41) Arsalis, A.; Nielsen, M. P.; Kær, S. K. Application of an improved operational strategy on a PBI fuel cell-based residential system for Danish single-family households. *Appl. Therm. Eng.* **2013**, *50*, 704−713.

(42) Kemp, I. *Pinch Analysis and Process Integration*, 2 ed.; Elsevier, 2006.

(43) Ersoz, A.; Sayar, A. A Process Simulation Study of a Newly Designed Fuel Processing System for a High Temperature PEM Fuel Cell Unit. *Int. J. Hydrogen Energy* **2015**, *40*, 14469−14482.

(44) Chippar, P.; Oh, K.; Kim, W. G.; Ju, H. Numerical analysis of effects of gas crossover through membrane pinholes in high-temperature proton exchange membrane fuel cells. *Int. J. Hydrogen Energy* **2014**, *39*, 2863−2871.

(45) Sadli, I. Modélisation par impédance d'une pile à combustible PEM pour utilisation en électronique de puissance. Ph.D. Dissertation, GREEN, University of Lorraine, Nancy, 2006. https://hal.archives-ouvertes.fr/tel-01752782 (accessed 2022 08 22).

(46) Jo, A.; Oh, K.; Lee, J.; Han, D.; Kim, D.; Kim, J.; Kim, B.; Kim, J.; Park, D.; Kim, M.; Sohn, Y. J.; Kim, D.; Kim, H.; Ju, H. Modeling and Analysis of a 5 kWe HT-PEMFC System for Residential Heat and Power Generation. *Int. J. Hydrogen Energy* **2017**, *42*, 1698−1714.

(47) Zhang, G.; Xie, B.; Bao, Z.; Niu, Z.; Jiao, K. Multi-phase simulation of proton exchange membrane fuel cell with 3D fine mesh flow field. *Int. J. Energy Res.* **2018**, *42*, 4697−4709.

(48) Larminie, J.; Dicks, A. *Fuel Cell Systems Explained*, 2nd ed.; John Wiley & Sons, 2013; pp 1−406.

(49) Siegel, C.; Bandlamudi, G.; Heinzel, A. Systematic character-ization of a PBI/H3PO4 sol−gel membrane—Modeling and simulation. *J. Power Sources* **2011**, *196*, 2735−2749.

(50) Nalbant, Y.; Colpan, C. O.; Devrim, Y. Development of a one-dimensional and semi-empirical model for a high temperature proton exchange membrane fuel cell. *Int. J. Hydrogen Energy* **2018**, *43*, 5939−5950.

(51) BASF. Proton-conductive membrane. https://www.basf.com/global/en/who-we-are/organization/group-companies/BASF_New-Business-GmbH/our-solutions/proton-conductive-membrane.html (accessed Aug 22, 2022).